

UNIVERSITY OF CALIFORNIA
RIVERSIDE

Field Investigation of the Environmental Energy Balance

A Thesis submitted in partial satisfaction
of the requirements for the degree of

Master of Science

in

Mechanical Engineering

by

PapaMagatte Diagne

August 2006

Thesis Committee:
Dr. Marko Princevac
Dr. Akula Venkatram
Dr. Guillermo Aguilar

Copyright by
PapaMagatte Diagne
2006

The Thesis of PapaMagatte Diagne is Approved:

Committee Chairperson

University of California, Riverside

ACKNOWLEDGEMENTS

I would like to thank my advisor Professor Marko Princevac for guiding me through the most challenging and rewarding educational experience of my life. The sharpening of my engineering skills over the past two years is largely due to Marko's unique ability to clearly convey to his students, his vast knowledge of advanced topics in thermo-fluid sciences. I would like to thank all my other committee members Professor Akula Venkatram and Professor Guillermo Aguilar for supporting me in the completion of my thesis. Additionally, I would like to thank my friends and colleagues in the department. Spending time with my new and sure to be lifelong friends was the support system that kept me going through the rough times. Special thanks to my dad Abdoulaye, mom Fatemeh, and sister Sheva. Thanks for pushing me to my full potential and giving me the confidence to soar.

ABSTRACT OF THE THESIS

Field Investigation of the Environmental Energy Balance

by

PapaMagatte Diagne

Master of Science, Graduate Program in Mechanical Engineering
University of California, Riverside, September 2006
Dr. Marko Princevac, Chairperson

The objective of this project is to model the constituents of the energy balance at the surface of the earth, for different surface types and better understand the how the constituents change depending on surface type. A linear regression analysis is used to developed models of sensible and latent heat as a function of net radiation. This will allow for the estimation of these terms by only measuring net radiation. Meteorological instrumentation was deployed at the UCR's Citrus Grove (Citrus) and CE-CERT site. Instruments at the grove were deployed above a large area covered with dirt and orange trees while instruments at the CE-CERT site were above a concrete surface with few short buildings. Previous work and the results of this project show that net radiation is a good predictor of sensible, latent, and ground flux terms. A linear regression analysis of the short and long wave terms of the overall net radiation and the gradients of these terms, my model is more accurate than Grimmond's Ground Model and the Penman-Monteith method.

TABLE OF CONTENTS

Page

LIST OF TABLES.....	vii
LIST OF FIGURES.....	ix
NOMENCLATURE.....	xii
ABSTRACT.....	v

CHAPTER	Page
1. INTRODUCTION.....	1
2. PREVIOUS WORK.....	2
2.1 Gradient Ground Storage Model.....	2
2.2 Modified Bowen Ratio Method.....	6
2.3 Temperature Dependent Bowen Ratio Method.....	9
2.4 Estimating Heat Fluxes by Monin-Obukhov Similarity.....	15
3. MEASUREMENT SITES.....	19
3.1 Citrus Site.....	19
3.2 CE-CERT Site.....	20
3.3 National Weather Service Climate Data.....	21
4. LOCAL METEOROLOGY.....	22
4.1 Sensible Heating.....	22
4.2 Latent Heating.....	23
4.3 Radiation - Reflection, Scattering, and Absorption.....	23
4.4 Expansion Cooling and Saturation.....	24
4.5 Adiabatic Processes.....	25
4.6 Potential Temperature.....	27

4.7	Atmospheric Stability.....	27
5.	RESULTS.....	29
5.1	Penman-Monteith Method.....	29
5.1.1	5 Minute Average Data: Citrus Data.....	31
5.1.2	1 Hour Average Data: Citrus Data.....	36
5.2	Grimmond Ground Model.....	39
5.2.1	5 Minute Averages: Citrus Data.....	41
5.2.2	1 Hour Averages: Citrus Data.....	44
5.3	Citrus Site vs. CE-CERT Site.....	46
6.	CONCLUSIONS.....	48
	APPENDIX A: INSTRUMENTATION.....	49
A.1	Water Content Reflectometer.....	49
A.2	HFP01SC Soil Heat Flux Plate.....	51
A.3	CSAT3 Sonic Anemometer.....	53
A.4	KH20 Krypton Hygrometer.....	55
A.5	CNR1 Net Radiometer.....	58
A.6	HMP45-C Relative humidity Probe.....	60
A.7	IRTS-P Infrared Temperature Sensor.....	61
A.8	CR 5000 DataLogger.....	62
	APPENDIX B: STATISTICAL ANALYSIS.....	64
B.1	Correlation and Covariance.....	64
B.2	Regression Analysis.....	65

B.2.1	Linear Regression.....	67
B.2.2	Polynomial Regression.....	71
B.2.3	Multiple Linear Regression.....	73
B.2.4	Non-linear Multiple Regression.....	75
B.3	Statistica.....	75
B.3.1	Beta weights.....	76
B.3.2	t-tests.....	76
B.3.3	R^2	76
B.3.4	Adjusted R^2	77
B.3.5	F -test	78
B.3.6	Stepwise Multiple Regression.....	78
REFERENCES.....		80

LIST OF TABLES

Table	Page
2.1. The dependence of the ratios γ/s and $(\lambda/s)/(1+\gamma/s)$ on temperature for standard pressure $P = 1000 \text{ mb}$.	11
5.1. Coefficients of Modified Grimmond model for Sensible Heat Flux.	31
5.2. Coefficients of Modified Grimmond model for Latent Heat Flux.	32
5.3. Errors of Holtslag, Modified Holtslag, and Modified Grimmond Models.	32
5.4. Coefficients of Modified Grimmond model for Sensible Heat Flux.	36
5.5. Errors of Holtslag, Modified Holtslag, and Modified Grimmond Models.	37
5.6. Coefficients of Grimmond Ground Model.	41
5.7. Coefficients of Modified Grimmond Ground Model.	41
5.8. R^2 values and Error for Grimmond Ground model and modified version.	41
5.9. Coefficients of Grimmond Ground Model.	44

5.10.	Coefficients of Modified Grimmond Ground Model.	44
5.11.	R^2 values and Error for Grimmond Ground model and modified version.	44
5.12.	Citrus Data Averages.	47
5.13.	CE-CERT Data Averages.	48
B.1.	Axis Transformations Used to Linearized Non-Linear Functions.	67

LIST OF FIGURES

Figure	Page
2.1. Cloudy daytime ground model based on Equation 2.3	4
2.2. Clear daytime ground model based on Equation 2.3	4
3.1. Citrus Grove Site courtesy of Google Earth	19

3.2.	Close-up	of	Citrus	Grove	Tower	Location	20
3.3.	CE-CERT	Site	courtesy	of	Google	Earth	21
3.4.	Close-up	of	CE-CERT	Tower	Location		21
5.1.	Modeling	of	Sensible	Heat	Flux	during clear daytime condition	32
5.2.	Modeling	of	Sensible	Heat	Flux	during cloudy daytime condition	33
5.3.	Modeling	of	Sensible	Heat	Flux	during general daytime condition	33
5.4.	Modeling	of	Sensible	Heat	Flux	during general nighttime condition	34
5.5.	Modeling	of	Latent	Heat	Flux	during clear day condition	34
5.6.	Modeling	of	Latent	Heat	Flux	during cloudy daytime condition	35
5.7.	Modeling	of	Latent	Heat	Flux	during general daytime condition	35
5.8.	Modeling	of	Latent	Heat	Flux	during general nighttime condition	36

5.9. Modeling of Sensible Heat Flux during clear daytime condition
37

5.10. Modeling of Sensible Heat Flux during cloudy daytime condition
38

5.11. Modeling of Sensible Heat Flux during general daytime condition
38

5.12. Modeling of Sensible Heat Flux during general nighttime condition
39

5.13. Clear Day Ground Models
42

5.14. Cloudy Day Ground Models
42

5.15. General Daytime Ground Models
43

5.16. General Nighttime Ground Models
43

5.17. Clear Day Ground Models (1-hr average)
45

5.18. Cloudy Day Ground Models (1-hr average)
45

5.19. Daytime Ground Models (1-hr average)
46

5.20. Nighttime Ground Models (1-hr average)

46

A.1. Picture of soil water content reflectometer with accuracy, resolution, and basic operating principle

49

A.2. Picture of soil heat flux plate with measurement range, accuracy, nominal signal range, and sensitivity

51

A.3. Schematic of soil heat flux plate, thermocouples and soil water content reflectometer.

51

A.4. Picture of sonic anemometer with measurement rate and error due to noise

53

A.5. Picture of krypton hygrometer with max frequency response

55

A.6. Picture of net radiometer with measurement range, spectral range, sensitivity, and expected daily error

58

A.7. Picture of relative humidity probe with humidity measurement range, humidity accuracy, temperature measurement range, and temperature measurement accuracy.....60

A.8. Picture of infrared temperature sensor with measurement range, accuracy, and response time
61

A.9. Picture of CR5000 datalogger
62

NOMENCLATURE

English

c_p	specific heat of air at constant pressure
c_v	specific heat of air at constant volume
c	speed of sound (metric)
G	ground flux
e	vapor pressure
g	gravitational acceleration
H	sensible heat flux
k	Von Karman constant
k_w	absorption coefficients for water vapor
L	Monin-Obukhov stability length
LE	latent heat flux
q_s	saturation specific humidity
q	specific humidity
Q^*	net radiation
S_u	short wave radiation measured from upper CM3 pyranometer
S_d	short wave radiation measured from lower CM3 pyranometer
L_u	long wave radiation measured from upper CG3 pyrgeometer
L_d	long wave radiation measured from lower CG3 pyrgeometer
Q_F	anthropogenic heat flux
R	Universal Gas Constant

R_e	residual energy
T_*	dimensionless temperature scale
T	temperature, K
T_s	sonic anemometer temperature
u, v	velocity in perpendicular directions parallel to surface of the earth
u_*	friction velocity
V	voltage
w	velocity in the vertical direction
z_{0m}	momentum surface roughness length
z_{0h}	heat surface roughness length
z_{0q}	humidity surface roughness length
z_{oh}	heat transfer roughness

Greek

α_s	surface albedo
β_o	bowen ratio
ε_s	surface emmissivity
ρ	density of air, $\text{kg}\cdot\text{m}^{-3}$
σ	standard deviation
τ	shear stress (normalized by density), $\text{m}^2\cdot\text{s}^{-2}$
Ψ_m, Ψ_h, Ψ_q	stability functions

μ	dynamic viscosity, Pa·s, kg·m ⁻¹ ·s ⁻¹
$\bar{\mu}$	mean
●	kinematic viscosity (momentum diffusivity), m ² ·s ⁻¹
-	potential temperature, K
λ	latent heat of vaporization of water

Subscripts

BREB	bowen ratio energy balance method
MBR	modified bowen ratio energy balance method

1.0 Introduction

The purpose of this thesis is twofold. The primary objective is to develop a simple model to accurately predict the components of the energy balance at the surface of the earth. The ideal model should have a minimal number of independent variables and terms. The secondary objective is to understand the effects of urbanization of the natural environment by comparing the constituents of the energy balance over two main types of surfaces; dirt and concrete. With the ability to understand and predict changes in the energy balance at the surface of the earth, we can continue to expand our cities while minimizing resulting phenomena like the urban heat island effect. Therefore I have analyzed flux measurements from the UCR Citrus Grove (dirt surface) and the CE-CERT parking lot (concrete surface).

Models of the sensible, latent and ground heat flux are created by a multiple linear regression. Since the physics of the energy balance show that radiation from the sun is the source for all other terms of the balance, it is the independent variable in the regression analysis. Specifically the four components of net radiation, and the gradients of these components, are implemented in the regression analysis. I have divided the data into four types: Cloudy Daytime, Clear Daytime, Night, and Day. Day or night is determined based on a positive or negative value of the net radiation at a given time. Cloudy and clear days are defined based on cloud cover data provided by the National Weather Service. Previous work on such modeling primarily implements the overall net radiation as opposed to the four components of net radiation, as the input for flux models. This approach is less accurate than the method I am proposing, which does include more terms. The tools used to quantify the differences between surface types (dirt and

concrete) are ratios of fluxes and ratios of radiation terms. Since the two data sets were gathered at different times, ratios must be used to in essence normalize the two data sets and minimize the meteorological effects of different seasons.

2.0 Previous Work

2.1 Gradient Ground Storage Model

If all other terms of the surface energy balance are independently evaluated or measured, the ground storage term G can be found as the residual:

$$G = Q^* - H - LE, \quad (2.1)$$

where Q^* is the net radiation, H is the sensible heat flux and LE is the latent heat. The approach used to model this residual value is to parameterize it in terms of the net all-wave radiation which is the driving force of the entire system. The equations presented here are essentially empirical derived from the measurements of the surface energy balance.

In many climate models the proportion of the surface energy input which is used to heat the ground is a simple fraction of the surface net all-wave radiation:

$$G = aQ^*, \quad (2.2)$$

where a is a constant. The first attempt to parameterize heat storage change in cities used a similar approach but incorporated an offset (Oke *et al.*, 1981). The next progression was a composite equation combining different urban surfaces into a composite equation. Each surface type is weighted according to their coverage area of the measurement area. The equation is of the form:

$$G = \sum_{i=1}^n \alpha_i (a_i Q^* + b_i) \quad (2.3)$$

where α_i is the fraction of the urban area covered by the i -th surface, a_i and b_i are constants. Although the storage model, Equation 2.3, is in reference to urban environments it can also be applied to other types of environments. The general performance of this linear model was satisfactory especially when used for periods of a day or more. However, it was unable to provide accurate hourly values at all times of the day because the linear form of the model do not allow it to match observed phase shifts between G and Q^* . These characteristics were confirmed by a more rigorous test (Oke and Cleugh, 1987). A more general form of Equation 2.3 is obtained by generalizing coefficients a_i and b_i to overall land type coefficients.

$$G = aQ^* + b \quad (2.3a)$$

These general coefficients are used for all of the heat flux models presented in this thesis. Applying Equation 2.3a to my data did not produce good results as shown in Figures 2.1 and 2.2. All error calculations are the average absolute difference between modeled and measured data.

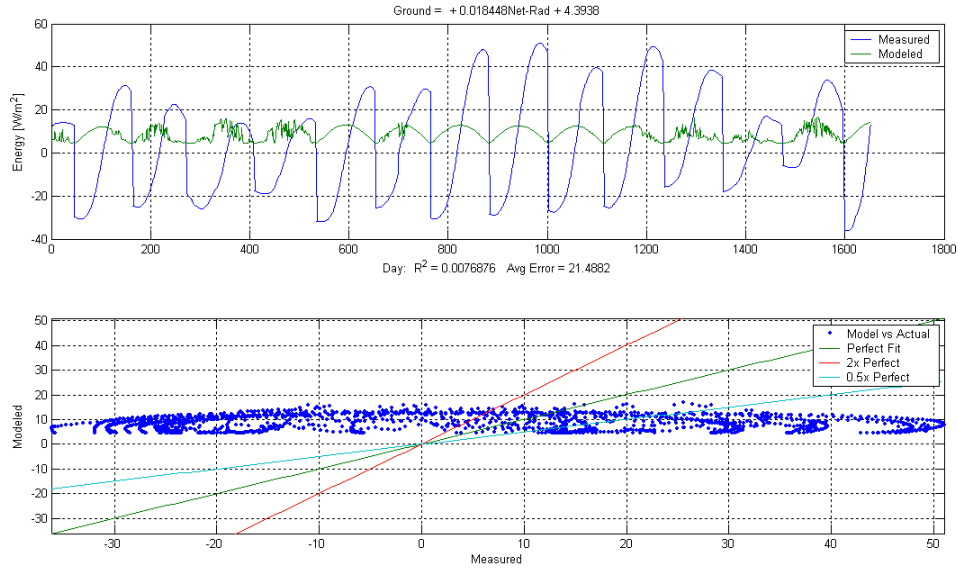


Figure 2.1: Daytime ground model based on Equation 2.3

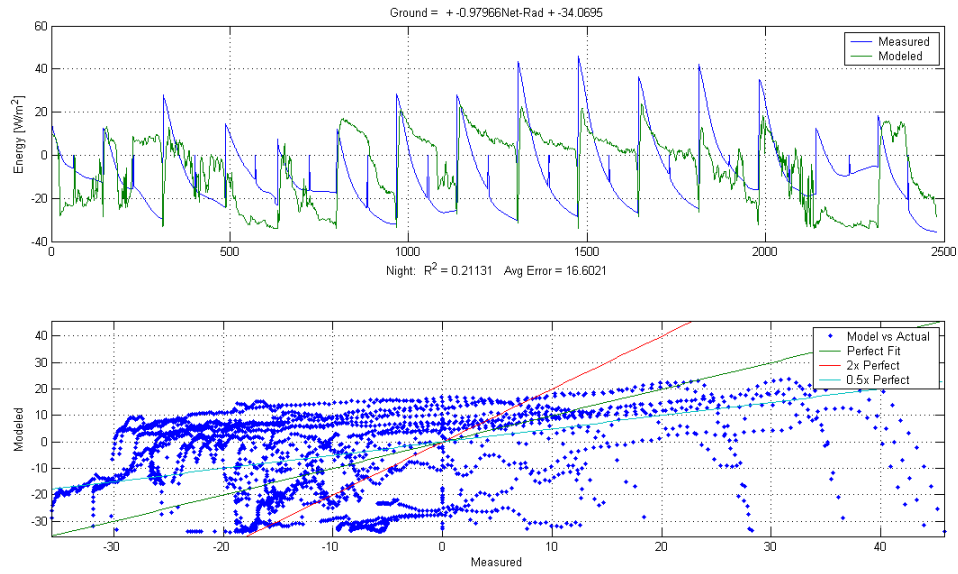


Figure 2.2: Nighttime ground model based on Equation 2.3

Several observational studies of homogeneous surfaces have investigated the relation between Q^* and G (Clothier *et al.*, 1986). Results of these studies show that the

assumption of a linear relationship between Q^* and G is false. Due to the observed phase shift between the two quantities, plots of net radiation and ground heat flux give a hysteresis loop. In other words, the relationship between Q^* and G , when Q^* is increasing, is different from when Q^* is decreasing. In order to account for this behavior Camuffo and Bernardi (1982) proposed the following form of equation:

$$G = a_1 Q^* + a_2 \frac{\delta Q^*}{\delta t} + a_3 \quad (2.4)$$

where t is time and a_1 , a_2 and a_3 are empirically determined coefficients. $\partial Q^* / \partial t$ has units of $Wm^{-2}h^{-1}$ and the coefficients a_1 , a_2 , and a_3 are dimensionless, hours and Wm^{-2} respectively. Thus, the soil heat flux is expressed both as a function of net all-wave radiation and the rate and direction of change of radiant forcing. Coefficients a_1 and a_3 perform the same role as a and b in Equation 2.3, but a_2 accounts for hysteresis.

Oke and Cleugh (1987) showed that the form of Equation 2.4 was appropriate to the case of heat storage in the city. A good statistical fit to their small data set from a suburban site in Vancouver, BC was obtained with $a_1 = 0.35$, $a_2 = 0.28 h$ and $a_3 = -40 Wm^{-2}$, with fluxes in units of Wm^{-2} .

A physical explanation for the hysteresis loop may be seen as the inertial effect and is discussed in the literature. Oke and Cleugh (1987) propose that in the morning hours, the atmosphere is relatively stable and the mixed layer is confined to a shallow layer before the nocturnal inversion is completely eroded. Hence sensible heat is transferred more readily into the soil. In the afternoon when the atmosphere is unstable, and the coupling

of the boundary and surface layers is greatest, the turbulent transfer of heat into the atmosphere is vastly more efficient than conduction into the soil.

Combining Equations 2.4 and 2.3 produces a good way of incorporating hysteresis. The combined approach consists of three parts. First, the area under study is surveyed to create an inventory of the building dimensions, the distribution of surface materials and information necessary to characterize the study area and to calculate the size of the anthropogenic heat release from the area. Second, independent data sets involving simultaneous measurements of net all-wave radiation and ground heat flux for the range of urban surface materials are used in a regression analysis to obtain the coefficients a_1 , a_2 and a_3 . Third, the contributions made by coefficients from each surface derived in the second part are weighted by the results in the first part to give an equation which is of the form:

$$\Delta Q_s = \sum_{i=1}^n \left\{ a_{1i} Q^* + a_{2i} \left(\partial Q^* / \partial t \right) + a_{3i} \right\} \quad (2.5)$$

where, when $\Delta t = 1$, $\partial Q^* / \partial t = 0.5 (Q_{i+1}^* - Q_{i-1}^*)$.

2.2 Modified Bowen Ratio Method

Sensible (H) and latent (LE) heat fluxes over a surface can be estimated using the energy balance equation and the Bowen-ratio, $B_o = H / LE$ (Foken *et al.*, 1997). Using the equations of the turbulent diffusion of heat and water based on the eddy covariance method and assuming similarity of the eddy diffusivities of heat and water vapor the Bowen ratio may be defined by finite differences as:

$$B_o = \frac{c_p}{\lambda} \cdot \frac{\Delta T}{\Delta q}, \quad (2.6)$$

where c_p the specific heat of air at constant pressure, λ is the latent heat of vaporization of water, q is specific humidity, T is temperature, z is height, and $\Delta T = T(z_2) - T(z_1)$, $\Delta q = q(z_2) - q(z_1)$. Using the Bowen ratio energy balance (BREB) method H and LE are estimated as:

$$H_{BREB} = \frac{B_o}{1 + B_o} (Q^* - G) \quad (2.7)$$

$$LE_{BREB} = \frac{1}{1 + B_o} (Q^* - G) \quad (2.8)$$

The advantage of BREB is the simple determination of the Bowen ratio according to Equation 2.6. But, because of the imbalance in the closure of the energy terms the available energy, $Q^* - G$, should be replaced by $Q^* - G - R_e$ where R_e is the residual energy. This error is very important, usually in the order of 20–30%, and is split accordingly in the Bowen ratio between the sensible and latent heat fluxes making it difficult to obtain both fluxes with high degree of accuracy using the BREB.

Heping and Thomas (2001) proposed a modified Bowen ratio (MBR) method to measure Bowen ratio according to Equation 2.6 and sensible heat flux by the eddy covariance method (Aubinet *et al.*, 2000) given as:

$$H_{BREB} = \rho c_p \overline{w' T'} \quad (2.9)$$

Where w' is the fluctuation of velocity in the vertical direction, ρ is the air density, and T' is the temperature fluctuation. Now, the latent heat is calculated as

$$LE_{MBR} = \frac{H_{MBR}}{B_o} \quad (2.10)$$

H_{BREB} in Equation 2.9 cannot be measured directly by a sonic anemometer because the sonic anemometer measures the sonic temperature T_s , which is nearly equal to the virtual temperature (please see instrumentation section, Section 3). However, the sonic derived sensible heat flux obtained by the sonic anemometer can be expressed according to the anemometer user's manual as:

$$\overline{w'T'_s} = \overline{w'T'} + 0.51 \cdot \overline{T} \cdot \overline{w'q'} - 2 \frac{\overline{T} \cdot \overline{u}}{c^2} \overline{u'w'} \quad (2.11)$$

where c is the speed of sound and q' is humidity fluctuation. The first term of the right-hand side of Equation 2.11 is the sensible heat flux and can be obtained by the eddy covariance method ($\overline{w'T'}$). The third term of the right-hand side of Equation 2.11 is small in unstable conditions but cannot be neglected in near-neutral situations (Schotanus *et al.*, 1983) where its value can be up to 20% of the flux. In the MBR method, sensible heat flux is determined using Equation 2.11, and written as $\left(\overline{w'T'}\right)_c$. The transformed sonic derived heat flux, $\left(\overline{w'T'}\right)_c$, from the sensible flux, $\overline{w'T'_s}$, is obtained by substituting the following into Equation 2.11:

$$\overline{w'q'} = \frac{c_p}{(\lambda \cdot B_o) \cdot \overline{w'T'}} \quad (2.12)$$

where u is the horizontal wind velocity. After the substitution:

$$\left(\overline{w'T'}\right)_c = \frac{\left[\overline{w'T'_s} + 2 \frac{\overline{T} \cdot \overline{u}}{c^2} \overline{u'w'}\right]}{\left[1 + \frac{0.51 \cdot \overline{T} \cdot c_p}{\lambda \cdot B_o}\right]} \quad (2.13)$$

$$H_{MBR} = \rho c_P \left(\overline{w' T'} \right)_c = \rho c_P \frac{\left[\overline{w' T'_s} + 2 \frac{\overline{T} \cdot \overline{u}}{c^2} \overline{u' w'} \right]}{\left[1 + \frac{0.51 \overline{T} \cdot c_P}{\lambda \cdot B_o} \right]} \quad (2.14)$$

The average sound speed can be replaced by (Schotanus *et al.*, 1983)

$$\overline{c^2} = a R \overline{T} (1 + 0.51 \overline{q}) \quad (2.15)$$

where R is the gas constant for dry air and $a = 1.4 = c_p/c_v$ is the ratio of specific heats under constant pressure and constant volume.

Finally, based on the determination of B_o according to Equation 2.6 and the sensible heat flux according to Equations 2.14 and 2.15, the latent heat flux can be determined by 2.10. Therefore a new equation has been derived to obtain H_{MBR} (Liu *et al.*, 2001) as follows:

$$H_{MBR} = \rho c_P \left(\overline{w' T'} \right)_c = \rho c_P \frac{\overline{w' T'_s} + \frac{2 \overline{T}}{c^2} \left(\overline{u} \cdot \overline{u' w'} \cdot A + \overline{v} \cdot \overline{v' w'} \cdot B \right)}{1 + \frac{0.51 \overline{T} \cdot c_P}{\lambda \cdot B_o}} \quad (2.16)$$

where A and B are correction factors, both equal to 7/8 for CSAT anemometers (see Section 3 for the instrumentation description).

2.3 Temperature Dependent Bowen Ratio Method

In 1977 De Bruin and Holtslag analyzed a set of micrometeorological data collected at Cabauw, in the central Netherlands, during the period May-August. The result of their work is an empirical model that gives hourly estimates of the surface fluxes of heat and momentum from routine weather data during the daytime. The model is designed for

grass surfaces, but contains parameters which take into account surface properties in general. The inputs for the surface flux models are an estimated net radiation, estimated ground flux, surface temperature, and two empirical constants dependent on the saturation of the ground. Input for the estimated net radiation are wind speed, air temperature, and total cloud cover. This estimated net radiation is the input for the very simple ground flux model. The input for the momentum flux estimate is the friction velocity in terms of the Monin-Obukhov similarity parameters.

As will be discussed in detail in Section 4, the surface energy budget relates the net radiation Q^* of the former section to the various heat fluxes at the earth's surface according to Equation 2.1. For a land surface G is mostly small compared with Q^* during the daytime. The authors used for G the very simple formulation according to Equation 2.2 where $c = 0.1$ is obtained for a grass covered surface in the Netherlands. However, this ground model is not very good when compared to the hysteresis model developed by Grimmond in 1991.

Holtslag and Van Ulden (1983) used a simplified Penman-Monteith approach to calculate the sensible and latent heat fluxes (Smith and Blackall, 1979). This simplified parameterization is written as:

$$H = \frac{(1 - \alpha) + (\gamma / s)}{1 + (\gamma / s)} (Q^* - G) - \beta , \quad (2.17)$$

$$LE = \frac{\alpha}{1 + (\gamma / s)} (Q^* - G) + \beta \quad (2.18)$$

where $s = \partial q_s / \partial T$, q_s being the saturation specific humidity, $\lambda = c_p / c_l$, and, α and β empirical parameters. The ratios γ/s and $(\lambda/s)/(1 + \gamma/s)$ are tabulated as a function of temperature at standard pressure in Table 2.1.

Table 2.1: The dependence of the ratios γ/s and $(\lambda/s)/(1 + \gamma/s)$ on temperature for standard pressure $P = 1000$ mb .

$T(^{\circ}C)$	γ/s	$(\lambda/s)/(1 + \gamma/s)$
-5	2.01	0.67
0	1.44	0.59
5	1.06	0.51
10	0.79	0.44
15	0.60	0.38
20	0.45	0.31
25	0.35	0.26
30	0.27	0.21
35	0.21	0.17

In order to evaluate H and LE using Equations 2.17 and 2.18 α and β must be specified. The parameter α accounts for the strong correlation of H and LE with $Q^* - G$, while the parameter β accounts for the uncorrelated part. Parameter α depends on the surface moisture condition since as when there is a lack of water, α decreases (De Bruin and Holtslag, 1982).

Knowing the heat flux from the previous part, the Obukhov stability parameter L and the surface momentum flux can be estimated. The momentum flux is defined as:

$$\tau = \rho u_*^2 \quad (2.19)$$

where u_* is the friction velocity. Applying Monin-Obukhov similarity theory u_* is related to the wind speed parallel to the surface of the earth u at the height z by:

$$u_* = ku \left[\ln(z/z_{0m}) - \psi_M(z/L) + \psi_M(z_{0m}/L) \right]^{-1} \quad (2.20)$$

where k is the von Karman constant ($k=0.41$), z_{0m} the surface roughness length, ψ_M a stability function defined under stable conditions as:

$$\psi_M = 2 \ln \left(\frac{1+x}{2} \right) + \ln \left(\frac{1+x^2}{2} \right) - 2 \tan^{-1}(x) + \frac{\pi}{2} \quad (2.21)$$

where

$$x = 1 + 5 \frac{z}{L} \quad (2.22)$$

The Obukhov stability parameter, also known as Monin-Obukhov length, is defined as:

$$L = \frac{\rho c_p T u_*^3}{kgH} \quad (2.23)$$

Here, g is the acceleration of gravity. From Equations 2.20 and 2.23 u_* and L can be solved by iteration when T , H , z_{0m} and w are known. The surface roughness length z_{0m} can be obtained from terrain classifications developed by Wieringa (1980). For example, for open flat terrain with grass and few isolated obstacles, $z_{0m} = 0.03$ m. To solve u_* and L the following procedure is used. The sensible heat flux H is estimated with net radiation measurements (measured or modeled), Equations 2.17 and 2.18 or measurements of the sensible heat flux. The measured 10m wind speed is used for w and for T the air temperature. The computation begins with an estimate for u_* by way of Equation 2.20, where initially $\psi_M = 0$ ($L = \infty$). Then with Equation 2.23 an estimate for L is obtained. With this estimate Equation 2.20 is used again to improve the estimate for u_* , and so on.

Another formulation of the Obukhov stability parameter is based on the definition of the sensible heat flux:

$$H = -\rho c_p u_* T_* \quad (2.24)$$

where

$$T_* = k\Delta T \left[\ln(z_2/z_1) - \psi_H(z_2/L) + \psi_H(z_1/L) \right]^{-1} \quad (2.25)$$

and

$$\psi_H = 2 \ln \left(\frac{1+x^2}{2} \right) \quad (2.26)$$

Finally substituting the Equation 2.24 into Equation 2.23 gives

$$L = \frac{T u_*^2}{kg T_*} \quad (2.27)$$

The fluxes H and τ can be obtained from the above equations starting with a prescribed value of the Obukhov stability parameter L . The authors used $L = -36$. Then u_* and T_* are calculated from Equations 2.20-2.22 and Equations 2.25-2.27. Using Equation 2.27, L is computed using the estimated values of u_* and T_* . The new value of L is substituted back into Equations 2.20-2.22 and Equations 2.25-2.27 to obtain improved values for u_* and T_* . This cycle is repeated until successive values of L do not change more than 5%. Then H and τ are calculated with 2.19 and 2.24.

Surface moisture parameters α and β are allow the model to be applied to a variety of ground cover types. With $\alpha = 1$ and $\beta = 10 \text{ Wm}^{-2}$ good results for the sensible heat flux H can be obtained for grass provided with enough water to evaporate. For bare soil, however, it is expected that $LE = 0$ when there is no water to evaporate. In 2.17 and

2.18 α and β are constants for given surface conditions. This can only be fulfilled by putting $\alpha = \beta = 0$ for $LE = 0$. Taking these limits for α and β they can be re-written as:

$$\beta = \beta' \alpha \quad (2.28)$$

Where β' is the value for which $\alpha = 1$. In general 2.18 may be rewritten for LE with the use of 2.22 as:

$$LE = \alpha \left[\frac{1}{1 + \gamma/s} (Q^* - G) + \beta' \right] \quad (2.29)$$

In general α can be computed by means of a regression analysis between observations of LE and $(Q^* - G)(1 + \gamma/s)^{-1} + \beta'$. The advantage of 2.29 is that only α depends on the surface moisture condition.

2.4 Estimating Heat Fluxes by Monin-Obukhov Similarity

Surface sensible and latent heat fluxes are sometime estimated by the Bowen ratio energy balance method (Fritschen and Simpson, 1989), and the profile method (Panofsky and Dutton, 1984). The Bowen ratio method uses vertical gradients of temperature and water vapor pressure, and surface energy budget measured by the surface energy balance but it does not use information provided by the similarity law and measurements of wind speed in the surface layer. A major limitation of the Bowen ratio is that it becomes computationally unstable when the Bowen ratio is in the vicinity of -1 . And a limitation of the profile method is that it uses the similarity law to compute surface heat fluxes, but does not use information provided by surface energy budget measurements. As a result the computed fluxes are often inaccurate.

In order to use the benefits of the two techniques, Stewart and Thom (1973) and Thom *et al.* (1975) combined them and proposed the energy budget determination of heat fluxes. In this method, the heat fluxes computed by profile-gradient formulae are corrected by a stability factor derived from surface energy balance and appropriate profile-gradient data. The method was expanded further by Hu and Qi (1991) who extended the method by incorporating the Monin-Obukhov stability functions. In this method, all variables are considered as deterministic quantities and model errors are also not taken into consideration. However, ignoring model errors is not a realistic approach considering the stochastic nature of the model variables. Taking into consideration the random fluctuations and subsequent the errors of observations and models as well, Xu and Qiu (1997) first proposed a ‘variational’ method (XQ’s method) to estimate surface heat fluxes. Even with this improvement the computed heat fluxes are still relatively

sensitive to measurement errors, especially the errors in the observations of air temperature.

Based on Monin-Obukhov similarity theory (Businger *et al.*, 1971), nine independent residual differences between the model's estimates and corresponding observations can be described by the following equations:

$$\delta u_i = \frac{u_*}{k} \left[\ln \left(\frac{z_i}{z_{0m}} \right) - \psi_m \left(\frac{z_i}{L} \right) + \psi_m \left(\frac{z_{0m}}{L} \right) \right] - u_i, i = 1, 2, 3, \quad (2.30)$$

$$\delta T_i = T_s + \frac{T_*}{k} \left[\ln \left(\frac{z_i}{z_{0h}} \right) - \psi_h \left(\frac{z_i}{L} \right) + \psi_h \left(\frac{z_{0h}}{L} \right) \right] - T_i, i = 1, 2, 3, \quad (2.31)$$

$$\delta q_i = q_s + \frac{q_*}{k} \left[\ln \left(\frac{z_i}{z_{0q}} \right) - \psi_q \left(\frac{z_i}{L} \right) + \psi_q \left(\frac{z_{0q}}{L} \right) \right] - q_i, i = 1, 2, 3. \quad (2.32)$$

Here T_* and q_* are flux temperature and humidity scale, respectively; T_s is surface skin temperature; (u_1, u_2, u_3) , (T_1, T_2, T_3) , and (q_1, q_2, q_3) are observed wind speeds, temperatures, and specific humidity at heights of $z_1 = 1 \text{ m}$, $z_2 = 4 \text{ m}$, $z_3 = 10 \text{ m}$; z_{0m}, z_{0h} and z_{0q} are roughness lengths for momentum, heat, and humidity; ψ_m, ψ_h and ψ_q are the stability functions. For the unstable case $T_* \leq 0$ or $L \leq 0$, based on Paulson (1970), Dyer and Hicks (1970), and Hicks (1976), the stability functions ψ_m and ψ_h are taken as:

$$\psi_m = 2 \ln \left(\frac{1+x}{2} \right) + \ln \left(\frac{1+x^2}{2} \right) - 2 \arctan(x) + \frac{\pi}{2}, \quad (2.33)$$

$$\psi_h = \psi_q = 2 \ln \left(\frac{1+x^2}{2} \right). \quad (2.34)$$

where x is defined by Equation 2.22. For the stable case $T_* \geq 0$ or $L \geq 0$, based on Holslag and DeBruin (1988) and Beljaars and Holslag (1991), the stability functions ψ_m and ψ_h are given by:

$$-\psi_m = a \frac{z}{L} + b \left(\frac{z}{L} - \frac{c}{d} \right) \exp \left(-d \frac{z}{L} \right) + \frac{bc}{d} \quad (2.35)$$

$$-\psi_{h,q} = \left(1 + \frac{2az}{3L} \right)^{3/2} + b \left(\frac{z}{L} - \frac{c}{d} \right) \exp \left(-d \frac{z}{L} \right) + \frac{bc}{d} - 1 \quad (2.36)$$

here, $a = 1$, $b = 0.667$, $c = 5$, $d = 0.35$. The stability function $\psi_q = \psi_h$ is assumed.

Residual error in the surface energy balance equation is denoted by:

$$R_e = Q^* - G - H - LE \quad (2.37)$$

Sensible heat flux is computed by Equation 2.24 and latent heat flux is computed as:

$$LE = -\rho \lambda u_* q_* \quad (2.38)$$

Ideally, the residual error should be zero in Equation 2.37. However, since the terms on right-hand side of Equation 2.37 are measured or calculated with some errors and energy absorption the right side of Equation 2.37 is not generally equal to zero. These errors as a whole are represented by the residual error on the left side of Equation 2.37.

In order to address all of the aforementioned issues of error and accuracy the authors of this article have developed a new cost function, formulated with a variational technique (VT). In this new cost function, physical constraints are introduced to ensure stability and reliability. The goal is to optimize five parameters $(u_*, T_*, q_*, T_s, q_s)$ so that values of wind speed, potential temperature, and specific humidity computed by the profile formulae approximate the corresponding observations at three heights, and the

computed fluxes should approximately satisfy the surface energy budget. The author's variational approach to estimate the five parameters is accomplished by minimizing the following cost function:

$$J(u_*, T_*, q_*, T_s, q_s) = \frac{1}{2} \left(\alpha_1 \sum_{i=1}^3 \delta u_i^2 + \alpha_2 \sum_{i=1}^3 \delta T_i^2 + \alpha_3 \sum_{i=1}^3 \delta q_i^2 + \alpha_4 R_e^2 \right) \quad (2.39)$$

where α_i are constants. The first three terms on the right side of Equation 2.39 measure the fits to the observed wind speeds, temperatures, and specific humidity at three heights. The last term measures the fit to the surface energy balance. According to maximum likelihood theory, weights $\alpha_1, \alpha_2, \alpha_3, \alpha_4$ in Equation 2.39 should be inversely proportional to variances of the corresponding model's errors plus observational errors (Lorenc, 1986), but it is very difficult to compute the variances of models. So the authors estimate the weights only according to observational errors determined by the accuracy of the instruments. The authors set $\alpha_1 = 4 \text{ m}^2\text{s}^{-2}$, $\alpha_2 = 25 \text{ K}^2$, $\alpha_3 = 2.055 \times 10^7$, and $\alpha_4 = 3.3 \times 10^{-3} \text{ W}^2\text{m}^4$. Optimizing the five parameters $(u_*, T_*, q_*, T_s, q_s)$ is done by an iterative process. After guessing initial values of u_*, T_*, q_*, T_s, q_s parameters such as the Monin-Obukhov length L , sensible heat flux H , latent heat flux LE , $\delta u_i, \delta T_i, \delta q_i, R_e$ and J are calculated. The appropriateness of the initial guesses are measured by calculating the gradient of J . If $|\nabla J| \leq 10^{-4}$ then the initial guesses are good, but if this convergence criteria is not satisfied, different initial values of u_*, T_*, q_*, T_s, q_s must be chosen.

3.0 Measurement Sites

3.1 Citrus Site

Data from the citrus site was collected over the month of February, 2006. The latitude and longitudinal coordinates of the site are N 33.58.412 W 117.2.661 with an elevation of 978 ft. Our instruments were setup on a pre-existing tower at the location marked in Figure 3.1 and 3.2. Immediately surrounding the tower (within a 15m radius) is a dirt area. To the east and south of the tower are 4.5m orange trees. To the north are apartment buildings and to the west a dirt field. The orange trees were watered twice a week which is apparent by the relative increase in the latent heat flux on the days of watering.



Figure 3.1: Citrus Grove Site photo by Google Earth



Figure 3.2: Close-up of Citrus Grove Tower Location

3.2 CE-CERT Site

Data from the CE-CERT site was collected over the month of July, 2006. The latitude and longitudinal coordinates of the site are N 33.59.972 W 117.20.128 with an elevation of 935 ft. Our instruments were setup on the support and maintenance structure of a non-operational reactor above concrete, Figure 3.3 and 3.4. To the west of the CE-CERT lot is park and to the south are a group of orange trees. North of the site is dominated by an urbanized environment. East of the site is made up of the natural environment. Mountains to the southeast of the site cause a notable increase in wind compared to the Citrus site.



Figure 3.3: CE-CERT Site photo by Google Earth



Figure 3.4: Close-up of CE-CERT Tower Location

3.3 National Weather Service Climate Data

In my analysis the meteorological and climate data was separated according to cloudy and clear days. This separation was determined by data from the National Weather Service (<http://www.weather.gov/climate/index.php?wfo=sgx>). The archived data known as the Preliminary Climatology Data, is collected at the Riverside Airport approximately 6 miles west of the citrus site. Cloud cover data is presented as an integer value from 0 to

10. A value of zero corresponds to a no cloud cover over the span of an entire day. A value of 10 corresponds to a complete cloud cover over the entire day. Unfortunately, the data doesn't include cloud cover measurements for the nighttime. In my analysis, days that had a cloud cover value of one or greater were considered cloudy.

The meteorological conditions at the Citrus Grove and CE-CERT are diverse. In order to accurately describe the similarities and differences of the two sites, a review of basic meteorology is necessary. The following chapter will sensible heating, latent heating, radiation (reflection, scattering and absorption), expansion cooling and saturation, adiabatic processes, potential temperature, atmospheric stability, temperature inversions, and the heat island effect. These concepts are fundamental to describing and understanding the surface energy budget.

4.0 Local Meteorology

4.1 Sensible Heating

The term sensible is used to describe the heat transfer mechanism because heat redistribution brought about by sensible heating can be “sensed”, as temperature changes. Sensible heating involves both conduction and convection. Heat is conducted from the relatively warm surface of the Earth to the cooler overlying air. As the lowest portion of the troposphere is heated by contact with the Earth's surface, the surrounding air, which is cooler and denser, sinks downward and forces the warmer, lighter air to rise. The net result is a transfer of heat via conduction and convection from the surface of the Earth into the troposphere.

4.2 Latent Heating

Latent heating refers to the movement of heat from one place to another as a consequence of changes in the phase of water. Depending on the specific type of phase change, water either absorbs heat from its environment or releases heat to its environment. The quantity of heat that is involved in phase changes is known as the latent heat.

4.3 Radiation - Reflection, Scattering, and Absorption

Reflection occurs at the interface between two different media such as air and cloud when some of the radiation striking the interface is thrown back. At such an interface, the angle of incident radiation equals the angle of reflected radiation. The fraction of incident radiation that is reflected by a surface is called the albedo of that surface. Albedo is expressed either as a fraction or a percentage of incident radiation. Within the atmosphere, the tops of clouds are the most important reflectors of radiation from the sun. The albedo of cloud tops depends primarily on cloud thickness and varies from under 40 percent for thin clouds (less than 50m thick) to 80 percent or more for thick clouds (more than 5000m thick). The average albedo for all cloud types and thickness is about 55 percent, and at any given time, clouds cover about 60 percent of the planet. Ground albedo measurements of our two measurement sites are the primary means of quantifying differences between the two.

Scattering is the dispersal of radiation in all directions. Both gas molecules and aerosols in the atmosphere scatter solar radiation but there are some important differences. Scattering by molecules is wavelength dependent. On the other hand, water droplets and ice crystals that compose clouds scatter visible solar radiation equally at all

wavelengths. This is why clouds appear white. Scattering of incoming radiation directly effects net radiation measurements which are the input for the heat flux models I've created. Partly cloudy days cause fluctuations in net radiation measurements and hazy/foggy days cause a decrease in the average net radiation. As a result, model types are broken up into different categories: clear and not-clear, for example.

Reflection and scattering within the atmosphere merely change the direction of incoming solar radiation. However, through absorption, radiation is converted to heat. Most absorption within the atmosphere is by oxygen, ozone, water vapor, and various aerosols. For example, warming in the upper stratosphere is due to absorption of solar ultraviolet radiation by ozone and oxygen. Although clouds are excellent reflectors they are poor absorbers of solar radiation. Clouds typically absorb less than 10 percent of the radiation that strikes the cloud top, although exceptionally thick clouds such as thunderclouds may absorb more. Within the atmosphere, the sum of the percentage of insulation that is absorbed plus the percentage reflected or scattered plus the percentage transmitted to the Earth's surface must equal 100 percent. This conservation of radiation is a fundamental aspect of the overall energy balance by providing the only source of incoming energy to the surface of the Earth.

4.4 Expansion Cooling and Saturation

The relative humidity is 100 percent at saturation, but it is possible for air to become supersaturated, that is, for the relative humidity to be greater than 100 percent. As the relative humidity approaches or exceeds saturation, however condensation or deposition of water vapor becomes more and more likely. Clouds are products of condensation or

deposition within the atmosphere. Hence, the probability of cloud development increases as the relative humidity approaches saturation.

Relative humidity increases in two ways: 1) When air is cooled, the saturation vapor pressure declines whereas the vapor pressure remains constant. 2) When water vapor is added to the air, the vapor pressure increases whereas the saturation vapor pressure remains constant. Similarly, an increase in relative humidity and decrease in temperature results from expansion. In fact, expansion cooling is the principal means of cloud formation in the atmosphere. Expansion cooling takes place when the pressure on a volume of air drops, as it does when air ascends in the atmosphere. As air ascends, it expands in the same way that a helium filled balloon expands as it drifts skyward. Conversely, when air is compressed, its temperature rises. Compressional warming thus occurs when air descends within the atmosphere.

4.5 Adiabatic Processes

Expansion cooling and compressional warming within the atmosphere are examples of adiabatic processes. If a rising air parcel is unsaturated and is not heated or cooled from outside, the expansional cooling is dry adiabatic. In a dry adiabatic process, radiation and conduction are not effective in adding heat to or removing heat from the air parcel. As the parcel rises and expands, pushes against the surrounding air and cools at a rate equal to the work required to complete the expansion. This cooling rate, called the dry adiabatic lapse rate amounts to 10°C for every 1000m of ascent.

Also, air parcels descending within the atmosphere can undergo compressional warming. Whether the parcel is unsaturated or initially saturated, the compressional

warming is adiabatic. The atmosphere compresses the air parcel and the parcel temperature at the dry adiabatic lapse rate (10°C for every 1000m of descent). The ascent and descent of unsaturated air parcels within the real atmosphere are usually very close to adiabatic, so the dry adiabatic lapse rate enables us to accurately predict the temperature change of unsaturated air as it moves upward and downward within the atmosphere.

Should rising air parcels cool to the point that the relative humidity approaches 100 percent and condensation or deposition takes place, the ascending air then no longer cools at the dry adiabatic rate. This is because latent heat that is liberated during condensation or deposition partially encounters the expansional cooling. Consequently, an ascending saturated air parcel cools more slowly than an ascending unsaturated air parcel. Rising saturated air parcels cool at the moist adiabatic lapse rate.

Although the dry adiabatic lapse rate is fixed in value, the moist adiabatic lapse rate varies with temperature. As mentioned earlier, temperature governs the rate of vaporization of water so that the saturation vapor pressure is directly proportional to temperature. Warm saturated air has a higher vapor pressure than cool saturated air. Thus, condensation or deposition in warm saturated air releases more latent heat than condensation or deposition in cool saturated air. The greater the quantity of latent heat released, the more the expansional cooling is offset, and the smaller is the moist adiabatic lapse rate. The moist adiabatic lapse rate ranges from about 4°C per 1000m for very warm saturated air to almost 9°C per 1000m for very cold saturated air. As long as an unsaturated air parcel continues to ascend, its temperature will drop and its relative humidity will approach saturation. Forces arising from density difference within the

atmosphere may either enhance or suppress this vertical motion of air. The net effect depends on the stability of the atmosphere. These adiabatic processes are key to understanding and calculating potential temperature.

4.6 Potential Temperature

Atmospheric stability will be explained further in the next section but for now let us say it is consequence of the buoyancy effects in the atmosphere. Buoyancy in the atmosphere causes parcels of air to oscillate through different heights by undergoing compression and expansion. When taking a temperature measurement, how can you tell if what you are measuring is the temperature at that height or merely a parcel of air from a different altitude passing over the instrument? This is where the concept of potential temperature comes into play. Potential temperature is defined as the temperature a parcel of dry air would have if brought adiabatically to a standard pressure level of 1000 mb. As such, the potential temperature presents the preserved quantity. The conversion from temperature to potential temperature takes into consideration the pressure of the air parcel at a given temperature. By calculating temperature in reference to standard atmospheric pressure, temperatures at any number of heights can be compared to each other.

4.7 Atmospheric Stability

As mentioned briefly in the previous section, an air parcel is subject to buoyant forces that arise from density differences between the parcel and the surrounding ambient air. According to the ideal gas law the warmer an air parcel is, the lower is its density. Parcels that are warmer than the ambient air rise, and parcels that are cooler than the ambient air sink. An air parcel continues to rise or sink until it reaches air of equivalent density. The atmospheric stability is determined by comparing the temperature change of

an ascending or descending air parcel with the temperature profile or sounding, of the ambient air layer in which the parcel ascends or descends. The cooling rate of a rising air parcel depends on whether the parcel is saturated or unsaturated, and the warming rate of a descending air parcel is 10°C per 1000m.

Within a stable air layer, an ascending air parcel becomes cooler than the ambient air, or a descending air parcel becomes warmer than the ambient air. For either upward or downward displacements, an air parcel in stable air is thus forced to return to its original altitude. Within an unstable air layer, an ascending air parcel becomes warmer than the ambient air and continues to ascend, or a descending air parcel becomes cooler than the ambient air and continues to descend. Stability can change as a consequence of local radiational heating or cooling, air mass advection, or large scale ascent or descent of air. On a clear and calm night, radiational cooling of the ground stabilizes the overlying air, whereas during the day, solar heating of the ground destabilizes the overlying air. An air mass is stabilized as it travels over a colder surface, and it is destabilized as it flows over a warmer surface. Radiation or advection can change stability by changing the temperature profile.

Atmospheric stability conditions can also be determined by the dry adiabatic and moist adiabatic lapse rates, which directly influence the vertical temperature profile. If the temperature of ambient air is dropping more rapidly with altitude than the dry adiabatic lapse rate, then the ambient air is unstable for both saturated and unsaturated air parcels and known as absolute instability. Conditional stability occurs if the rate of temperature change of ambient air is between the dry adiabatic and moist adiabatic lapse rates. The air layer is stable for unsaturated air parcels and unstable for saturated air

parcels. An air layer is stable for both saturated and unsaturated air parcel when the ambient air is under any of the following conditions. (1) The temperature of the ambient air drops more slowly with altitude than the moist adiabatic lapse rate. (2) The temperature is constant with altitude (3) The temperature increases with altitude. Any one of these three categories of temperature profiles is a case of absolute stability.

In the case when the potential temperature change of ambient air equals the dry adiabatic lapse rate the ambient air is neutral for unsaturated air parcels and unstable for saturated air parcels. When the temperature change is the same as the moist adiabatic lapse rate, a neutral condition for saturated air parcels and stable for unsaturated air parcels results. Within a neutral air layer, a rising or descending air parcel always has the temperature of its surroundings. Therefore, a neutral air layer neither impedes nor hinders vertical motion.

Atmospheric stability influences weather by affecting the vertical motion of air. Stable air suppresses vertical motion, and unstable air enhances vertical motion, convection, expansional cooling, and cloud development. Because stability also affects the rate at which polluted air mixes with clean air, stability must be considered in assessing air pollution potential.

5.0 Results

5.1 Penman-Monteith Method

A physically realistic way to determine the partitioning of H and LE is the Penman-Monteith approach. A problem with this approach is that it is complicated and that several input parameters are needed which are difficult to obtain. For instance, the

surface resistance for latent heat is needed. Although several attempts are made in the literature to evaluate this surface resistance by means of empirical rules (Smith and Blackall, 1979) show that the Penman-Monteith approach can be simplified in such a way that it becomes more suitable in the presented context of this paper. The results of the simplification are Equations 2.17 and 2.18. The inputs to this model are net radiation and ground surface temperature. Therefore, some sort of model for the ground flux must be incorporated without introducing any additional independent variables. Equation 2.2 is such a model. However, this very simple model does not accurately represent the ground flux term. In order to evaluate H and LE by way of Equations 2.17 and 2.18 α and β must be specified. The parameter α accounts for the strong correlation of H and LE with $Q^* - G$, while the parameter β accounts for the uncorrelated part. Parameter α depends on the surface moisture condition since as when there is a lack of water, α decreases (De Bruin and Holtslag, 1982). For grass covered surface $\alpha = 1$. And, for prairie grass $\alpha = 0.45$. In the following analysis $\alpha = 0.7$ is used.

The purpose of this section is to compare my proposed improvement of Grimmond's ground flux equation (Equation 5.1) with the Penman-Monteith approach (Equations 2.17 and 2.18). The lower subplot of figures 5.1 through 5.12 shows the direct comparison between the two methods. The average error of my approach is lower than the Penman-Monteith method but this could be due to the poor choice of ground flux parameterization proposed by Holtslag. To illustrate the effects of the choice of ground model the upper subplot of each of the figures shows Penman-Monteith method first using ground flux by Equation 2.4 then using ground model as a factor of net radiation Equation 2.2. The difference in error between using the two different ground flux models is not great

enough to confirm that my proposed method is better than the Penman-Monteith method simply because of a poor choice in the ground flux model.

Net radiation measurements from the net radiometer are made up of four terms. They are short wave radiation from the upper CM3 pyranometer S_u , short wave radiation from the lower CM3 pyranometer S_d , long wave radiation from the upper CG3 pyrgeometer L_u , and long wave radiation from the lower CG3 pyrgeometer L_d . The all wave net radiation is simple the sum of the net short and net long wave radiation (it should be noted that measurements from the lower CM3 and CG3 are negative):

$$Flux = a_1 S_u + a_2 S_d + a_3 L_u + a_4 L_d + a_5 \frac{\delta S_u}{\delta t} + a_6 \frac{\delta S_d}{\delta t} + a_7 \frac{\delta L_u}{\delta t} + a_8 \frac{\delta L_d}{\delta t} + a_9 \quad (5.1)$$

5.1.1 5 Minute Average Data: Citrus Data

Tables 5.1 and 5.2 include the coefficients for the Sensible and Latent heat flux models for 5-minute averaged data. And, table 5.3 includes the errors of the Hottel, modified Hottel, and modified Grimmond models. The error is calculated as the average absolute difference between model and measured values. Figures 5.1-8 display results of sensible and latent flux models.

Table 5.1: Coefficients of Modified Grimmond model for Sensible Heat Flux

	Clear Day	Cloudy Day	Day	Night
a_1	0.65988	-0.0046446	0.5542	0.31921
a_2	-1.3614	1.5231	-0.71594	-0.27052
a_3	-0.63811	0.43128	-0.22101	1.011
a_4	0.0062783	-0.054344	-0.40504	-1.2835
a_5	-0.72253	-0.22641	-1.2414	-3.4517
a_6	5.6391	2.8631	7.2465	15.5444
a_7	-1.5773	1.4911	1.2893	6.7784
a_8	-12.0141	-10.2821	-14.9542	-21.1418

a_9	272.8816	-196.531	297.6746	157.0076
-------	----------	----------	----------	----------

Table 5.2: Coefficients of Modified Grimmond model for Latent Heat Flux

	Clear Day	Cloudy Day	Day	Night
a_1	-0.30162	0.22015	-0.21494	-0.40409
a_2	1.5336	-0.76933	1.1085	2.0831
a_3	0.25993	0.77675	0.30361	-0.45953
a_4	0.28594	-0.88542	0.15501	0.59384
a_5	-0.15112	-2.3816	-0.7718	0.78266
a_6	3.4104	13.1902	4.521	-4.9864
a_7	-7.9621	-1.6734	-3.0164	-3.993
a_8	7.9125	-2.9984	4.9694	9.5425
a_9	-275.1447	110.6315	-225.4435	-82.0194

Table 5.3: Errors of Holtslag, Modified Holtslag, and Modified Grimmond Models

	Holtslag Error, Wm^{-2}	Modified Holtslag Error, Wm^{-2}	Modified Grimmond Error, Wm^{-2}
Sensible: Clear Day	76.7103	86.5058	38.7777
Sensible: Cloudy Day	72.6907	78.4008	47.3809
Sensible: Day	78.2433	89.4677	50.9029
Sensible: Night	37.2966	28.0286	15.8443
Latent: Clear Day	160.3408	168.1075	38.4787
Latent: Cloudy Day	123.8881	125.7639	66.8174
Latent: Day	130.9225	141.7557	52.023
Latent: Night	20.8528	22.1696	22.1221

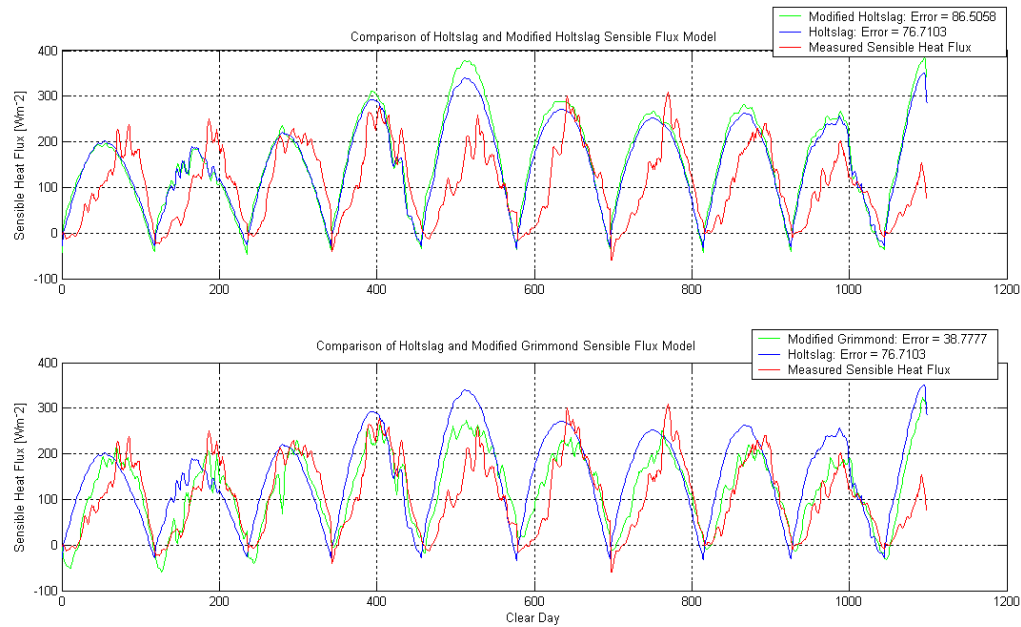


Figure 5.1: Modeling of Sensible Heat Flux during clear daytime condition

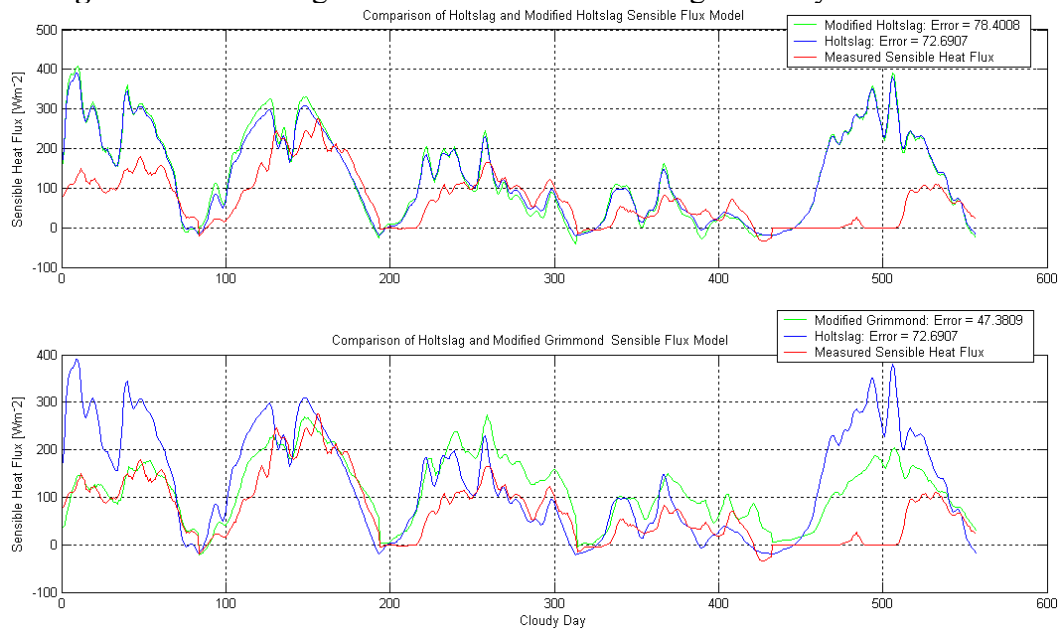


Figure 5.2: Modeling of Sensible Heat Flux during cloudy daytime condition

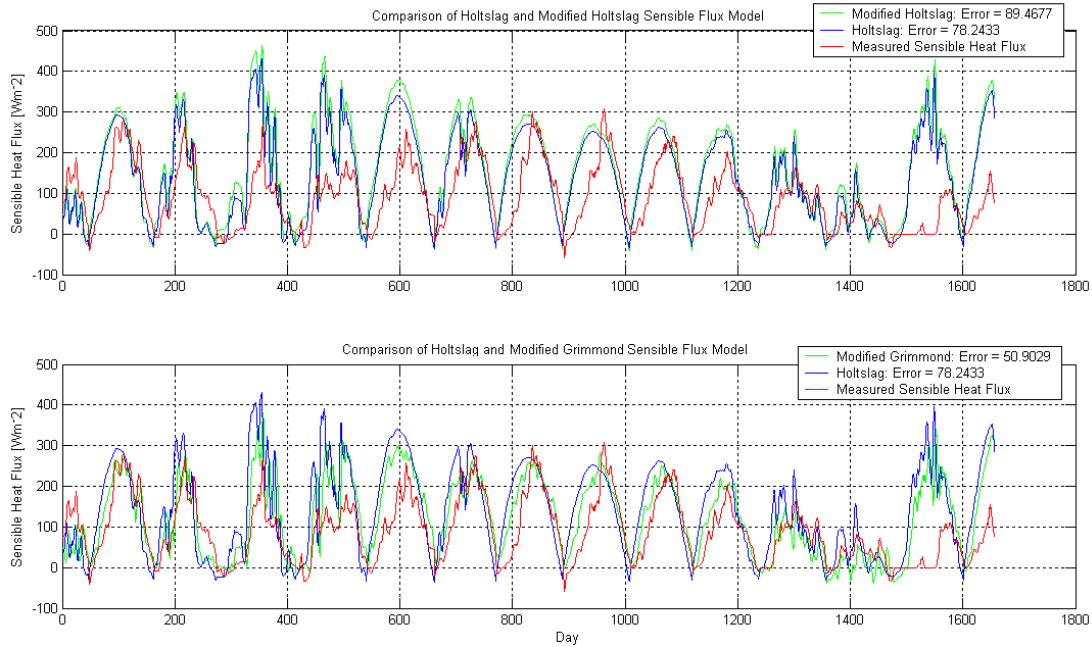


Figure 5.3: Modeling of Sensible Heat Flux during general daytime condition

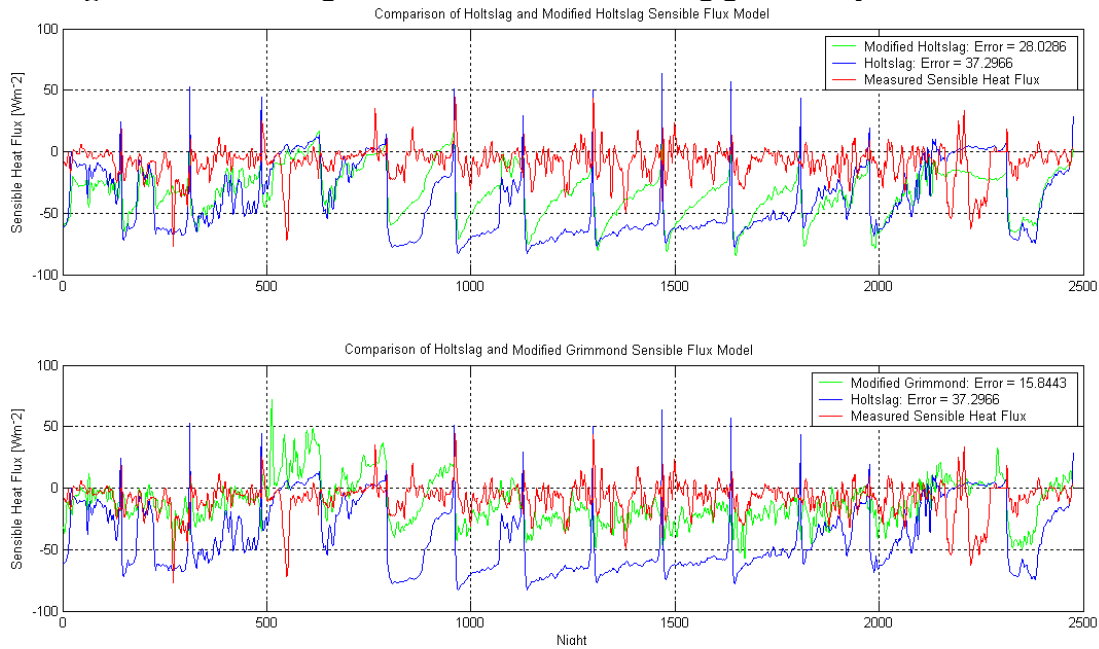


Figure 5.4: Modeling of Sensible Heat Flux during general nighttime condition

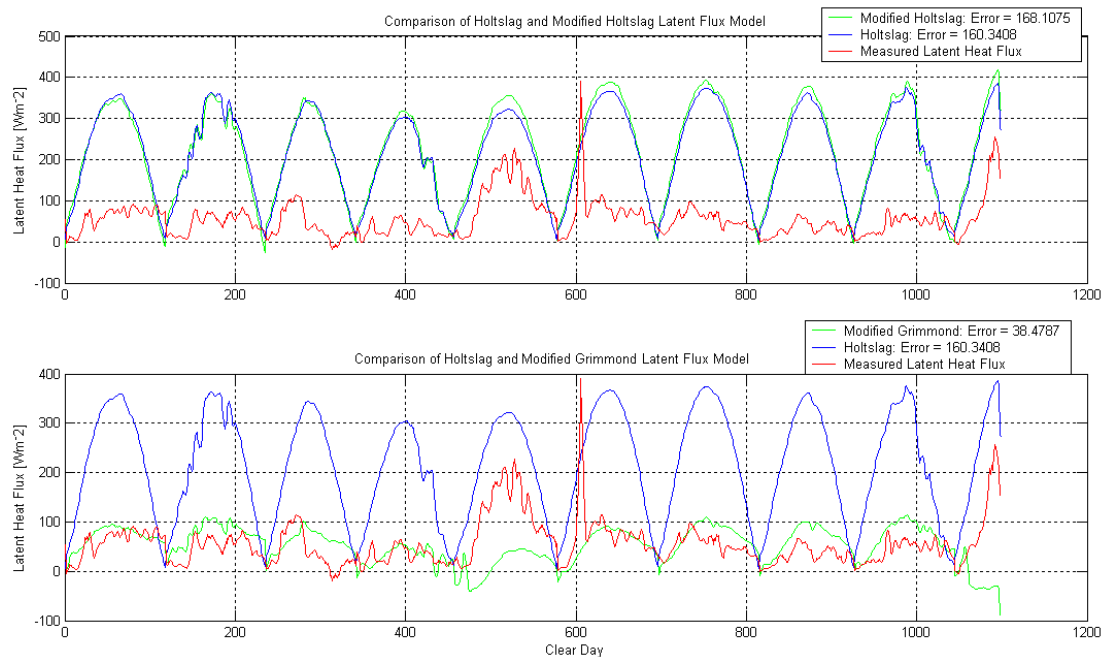


Figure 5.5: Modeling of Latent Heat Flux during clear day condition

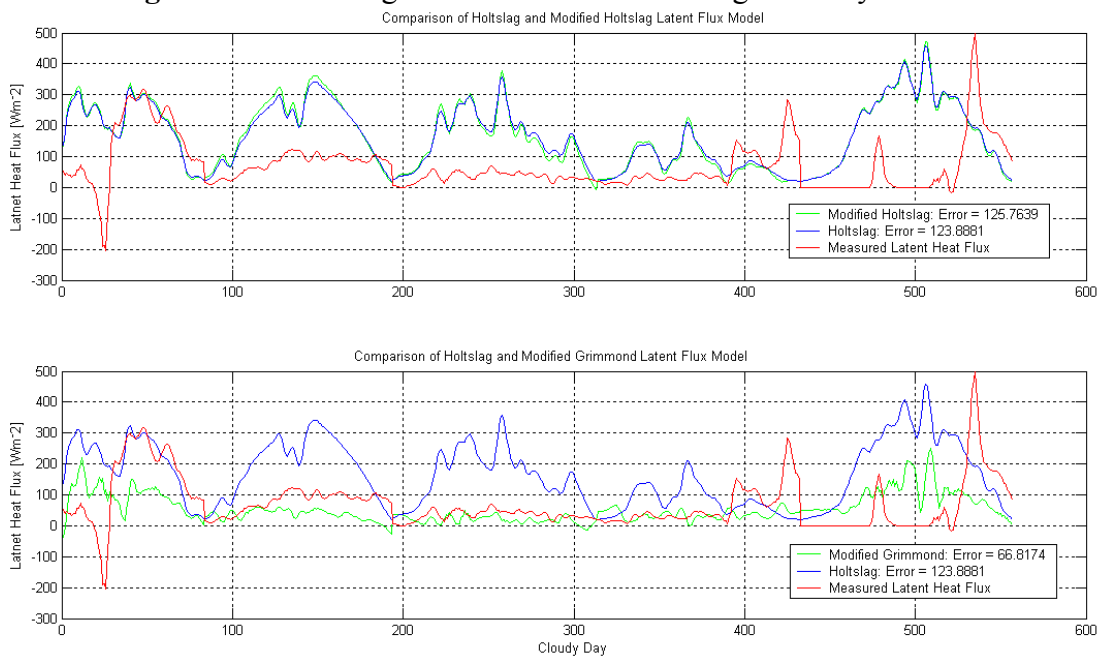


Figure 5.6: Modeling of Latent Heat Flux during cloudy daytime conditions

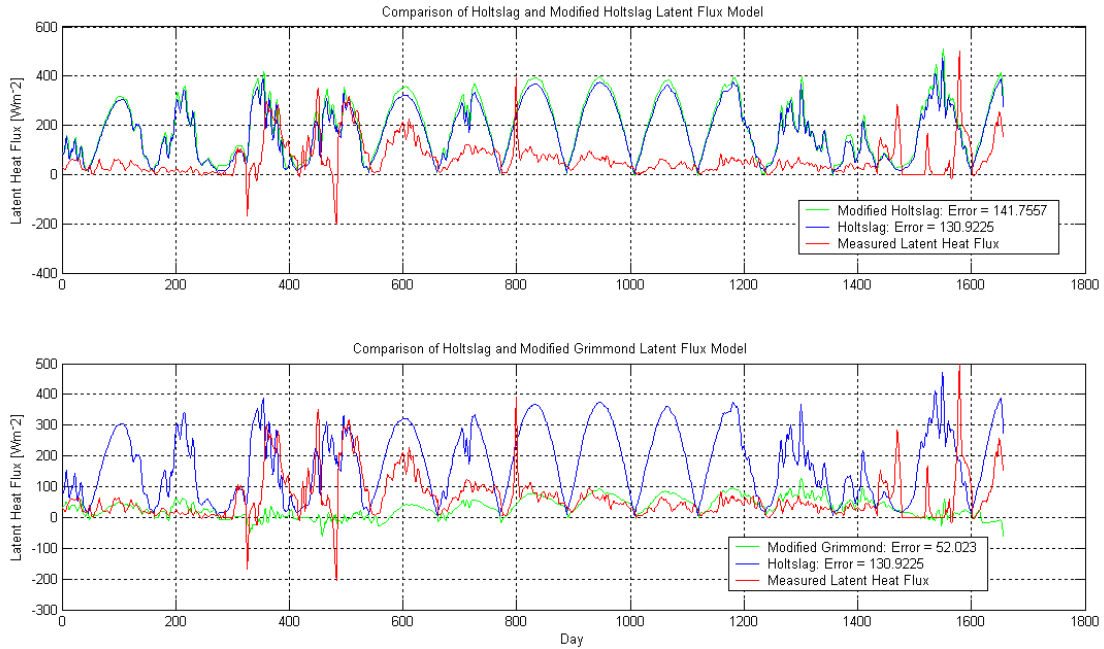


Figure 5.7: Modeling of Latent Heat Flux during general daytime conditions

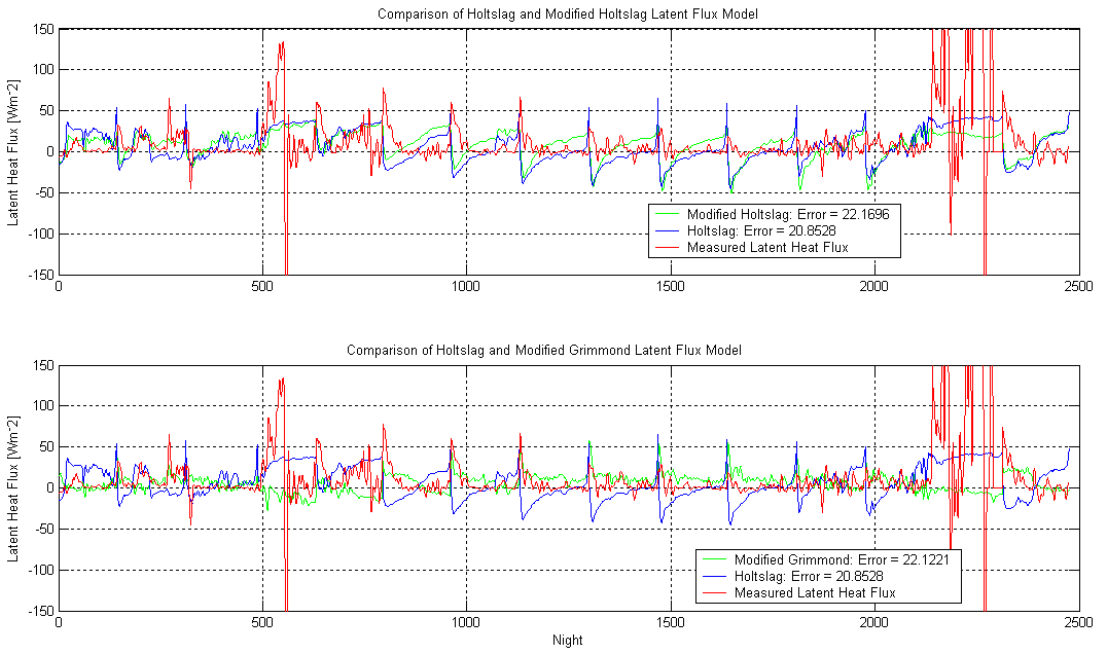


Figure 5.8: Modeling of Latent Heat Flux during general nighttime condition

5.1.2 1 Hour Average Data: Citrus Data

Table 5.4 includes coefficients for the Sensible heat flux model for 1-hour averaged data. Table 5.5 includes the errors of the Holtslag, modified Holtslag, and

modified Grimmond models. The error is calculated as the average absolute difference between model and measured values. Figures 5.9-12 display sensible flux models.

Table 5.4: Coefficients of Modified Grimmond model for Sensible Heat Flux

	Clear Day	Cloudy Day	Day	Night
a_1	0.7789	0.023063	0.5943	2.3118
a_2	-1.8883	1.2413	-0.89094	-8.454
a_3	0.23992	0.32222	0.15118	0.59053
a_4	-1.0868	0.037824	-0.98206	-0.88539
a_5	0.067368	-0.0017286	-0.1218	0.075495
a_6	-1.0658	0.34866	-0.070821	-0.054912
a_7	-1.1949	-0.11805	-1.2117	0.90548
a_8	-0.19273	-0.78911	-0.10986	-2.0635
a_9	316.2048	-128.5297	307.8921	122.4474

Table 5.5: Errors of Holtslag, Modified Holtslag, and Modified Grimmond Models

	Holtslag Error, Wm^{-2}	Modified Holtslag Error, Wm^{-2}	Modified Grimmond Error, Wm^{-2}
Sensible: Clear Day	60.1516	62.886	26.8117
Sensible: Cloudy Day	56.2958	60.1717	30.5322
Sensible: Day	59.9752	64.1143	43.6743
Sensible: Night	31.3466	31.3466	9.1151

Since the 5 minute averaged data shows that the modified Grimond model does not accurately predict latent heat fluxes, the 1 hour data average analysis does not include latent heat flux models.

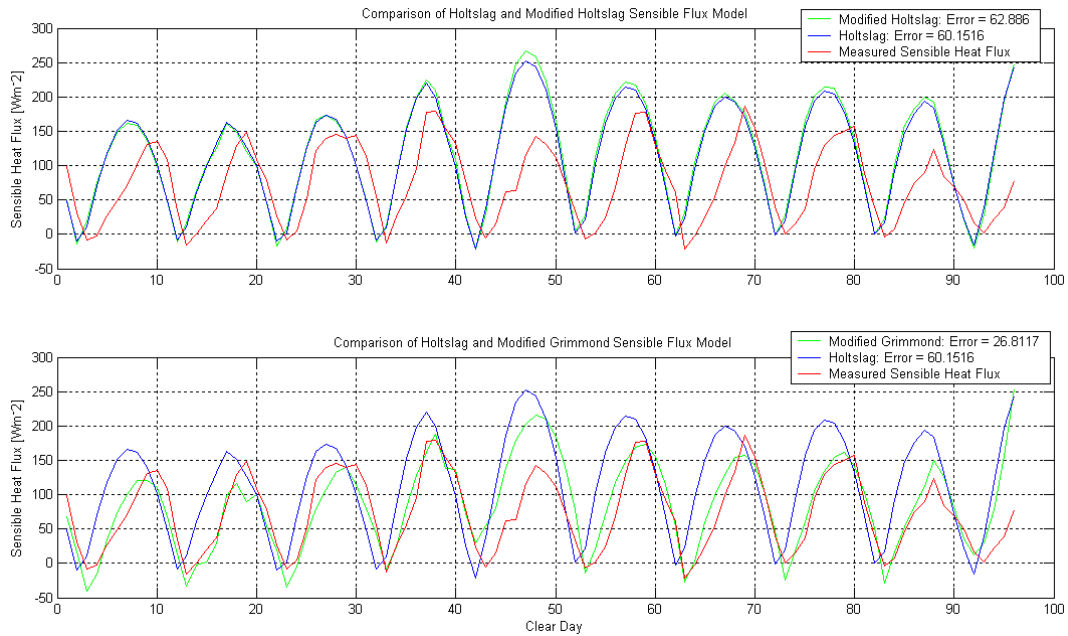


Figure 5.9: Modeling of Sensible Heat Flux during clear daytime condition

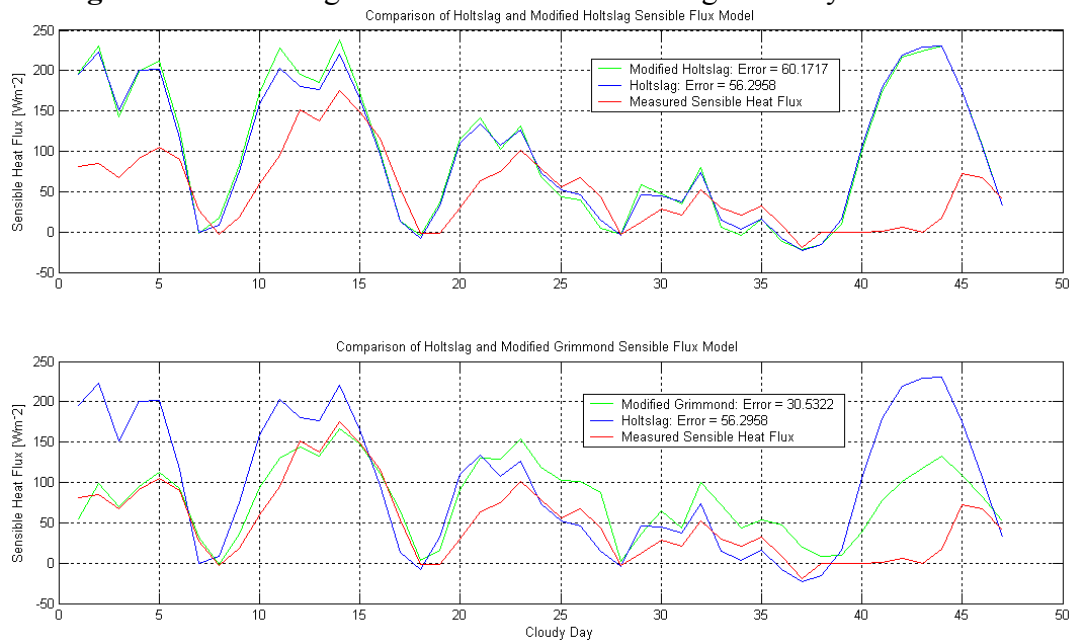


Figure 5.10: Modeling of Sensible Heat Flux during cloudy daytime condition

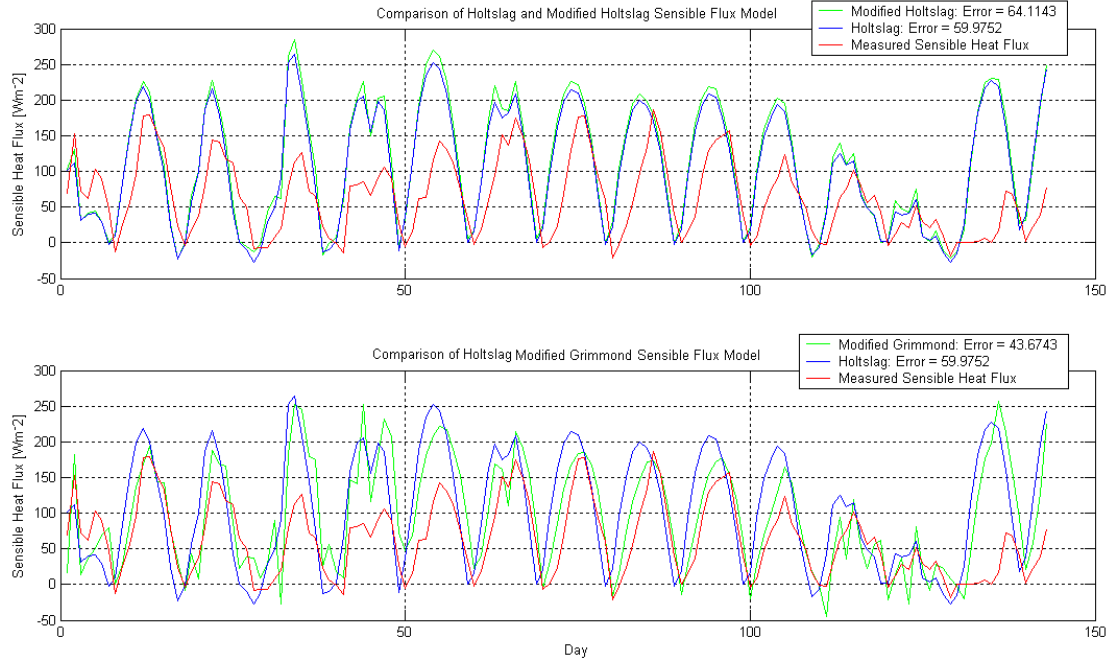


Figure 5.11: Modeling of Sensible Heat Flux during general daytime condition

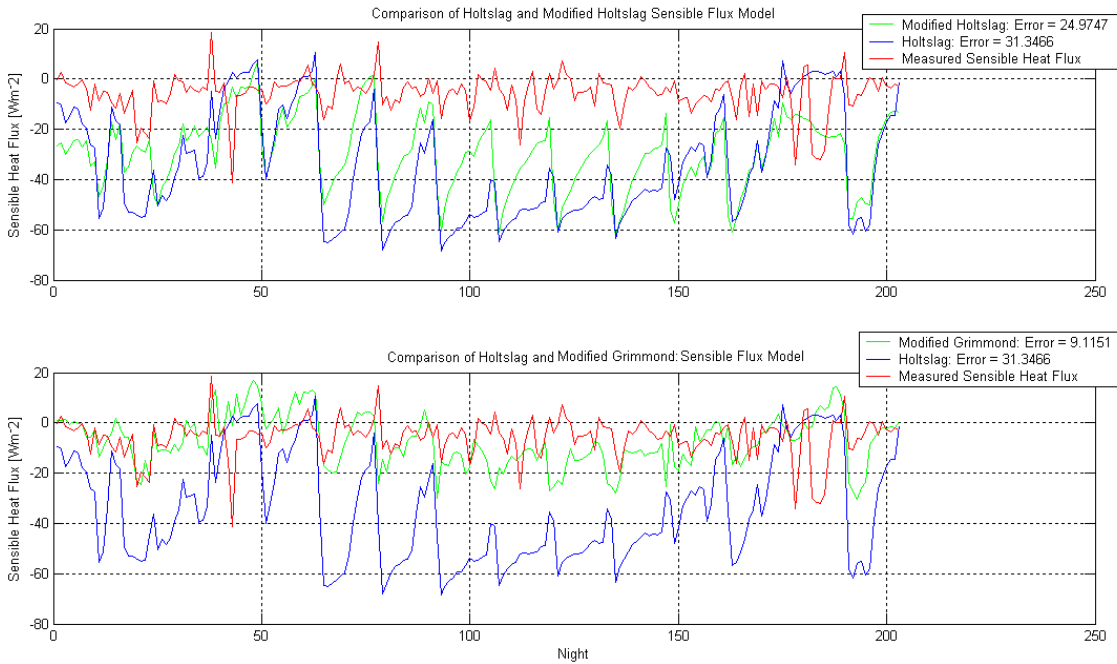


Figure 5.12: Modeling of Sensible Heat Flux during general nighttime condition

5.2 Grimmond Ground Model

The independent variables of Grimmond's ground model are net radiation (Q^*) and the derivative of net radiation with respect to time:

$$\Delta Q_s = a'_1 Q^* + a'_2 \frac{\partial Q^*}{\partial t} + a'_3 \quad (5.6)$$

I've applied this model to the Citrus data using a linear regression to solve for coefficients a'_1 , a'_2 and a'_3 (see figure 5.13). The quantity $\partial Q^* / \partial t$ is evaluated by forward differencing. Table 5.1 shows the coefficients resulting from the regression analysis.

Figures 5.13, 5.15, 5.17 and 5.19 are models of the four main meteorological conditions under consideration (clear day, cloudy day, overall day and overall night) using Grimmond's model. Figures 5.14, 5.15, 5.18 and 5.20 are the modified model. Included in the plots are the R^2 values and error calculations for each model. Error is calculated as the average absolute difference between measured and modeled quantities. I've modified her model by breaking up the net radiation term into more fundamental components. Table 5.8 summarizes the results of both models and shows the modifications are an improvement on Grimmond's model.

As mentioned in this section and the instrumentation section, net radiation is made up of four terms:

$$Q^* = S_u + S_d + L_u + L_d \quad (5.7)$$

Substituting Equation 5.7 into 5.6 gives:

$$\Delta Q_s = a'_1 (S_u + S_d + L_u + L_d) + a'_2 \frac{\partial}{\partial t} (S_u + S_d + L_u + L_d) + a'_3 \quad (5.8)$$

Distributing coefficients and the derivative gives:

$$\Delta Q_s = a'_1 S_u + a'_1 S_d + a'_1 L_u + a'_1 L_d + a'_2 \frac{\partial S_u}{\partial t} + a'_2 \frac{\partial S_d}{\partial t} + a'_2 \frac{\partial L_u}{\partial t} + a'_2 \frac{\partial L_d}{\partial t} + a'_3 \quad (5.8)$$

Finally, an assumption is made about the coefficients of each term. The modified model assumes that none of the coefficients are necessarily the same, *i.e.*

$$\Delta Q_s = a_1 S_u + a_2 S_d + a_3 L_u + a_4 L_d + a_5 \frac{\delta S_u}{\delta t} + a_6 \frac{\delta S_d}{\delta t} + a_7 \frac{\delta L_u}{\delta t} + a_8 \frac{\delta L_d}{\delta t} + a_9. \quad (5.9)$$

The idea behind this assumption is based on the linear regression analysis. By assuming the coefficients are different the model has greater flexibility in attempting to match the measured data. An advantage of the modified model is that it does not introduce any new measurements. It simply uses more fundamental elements of net radiation. It is not immediately apparent what any major disadvantages may result from increasing the number of terms in the model from three to nine. Table 5.7 summarizes the resulting coefficients of the regression analysis.

5.2.1 5 Minute Averages: Citrus Data

Table 5.6 and 5.7 include the regression coefficients of the 5 minute averaged Grimmond and Modified Grimmond models. Table 5.8 includes the errors of the two models. Figures 5.13-16 display ground flux models.

Table 5.6: Coefficients of Grimmond Ground Model

	Clear Day	Cloudy Day	Day	Night
a'_1	0.016528	0.0012089	0.015128	-0.97647
a'_2	-1.7247	-0.33744	-1.7267	-5.3511
a'_3	6.2988	0.25524	7.0093	-48.5666

Table 5.7: Coefficients of Modified Grimmond Ground Model

	Clear Day	Cloudy Day	Day	Night
a_1	-0.030352	0.078107	0.02433	0.029714
a_2	-0.19142	-0.82684	-0.50402	-1.3214
a_3	-0.69675	-0.32302	-0.73757	-0.36049
a_4	0.99001	0.73416	0.98381	1.0441

a_5	-0.062438	-0.10785	-0.48807	-0.95545
a_6	1.5189	1.5654	2.9225	4.5104
a_7	-2.3323	-0.48917	-0.015581	4.4013
a_8	-3.3928	-2.8662	-4.7772	-6.3168
a_9	-189.038	-222.3178	-159.4869	-373.2589

Table 5.8: R^2 values and Error for Grimmond Ground model and modified version

	Modified Grimmond, Error, Wm^{-2}	Grimmond, Error, Wm^{-2}	Modified Grimmond, R^2	Grimmond, R^2
Clear Day	18.3996	22.2989	0.84053	0.46798
Cloudy Day	17.9952	22.3493	0.76929	0.097873
Day	26.1328	28.9875	0.84734	0.46188
Night	10.4358	23.1054	0.92408	0.39177

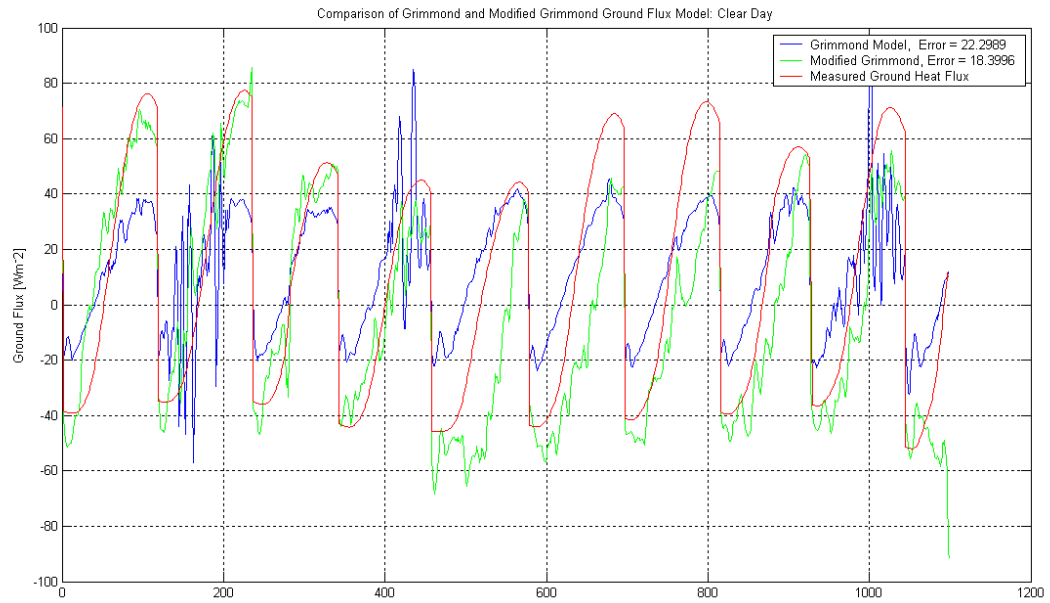


Figure 5.13: Clear Day Ground Models

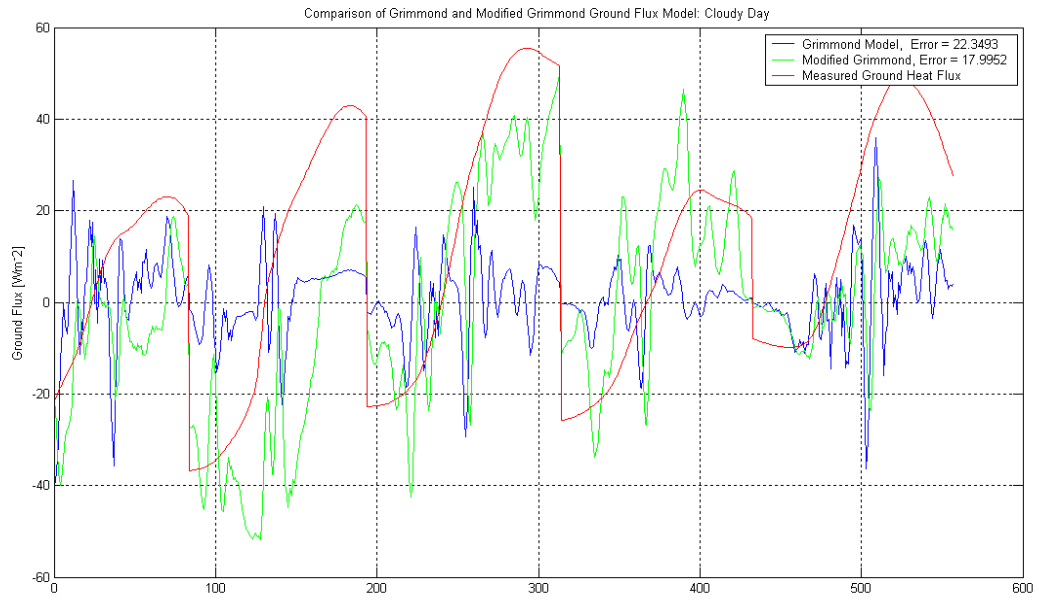


Figure 5.14: Cloudy Day Ground Models

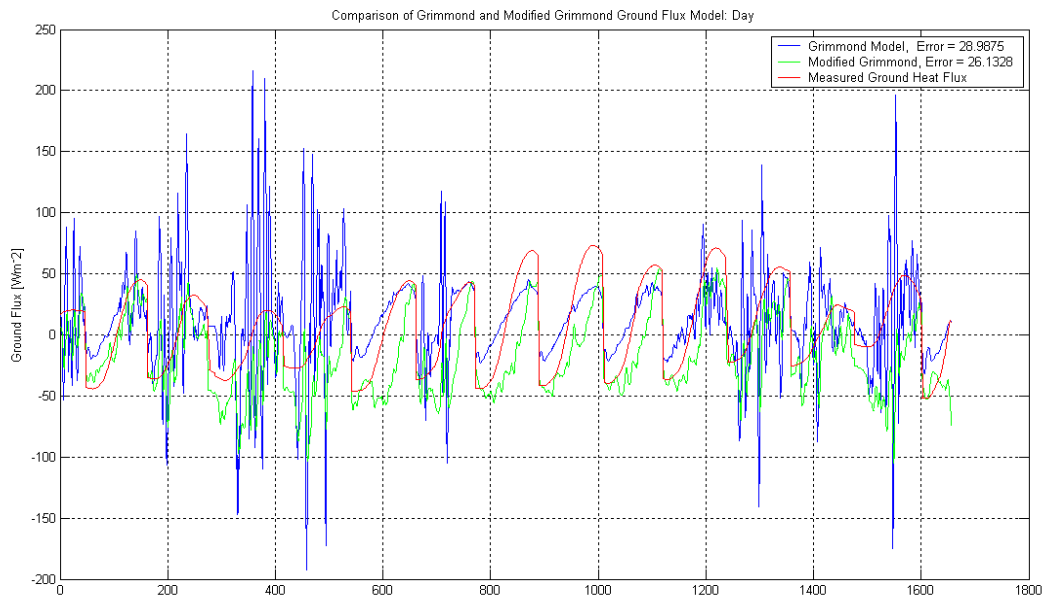


Figure 5.15: General Daytime Ground Models

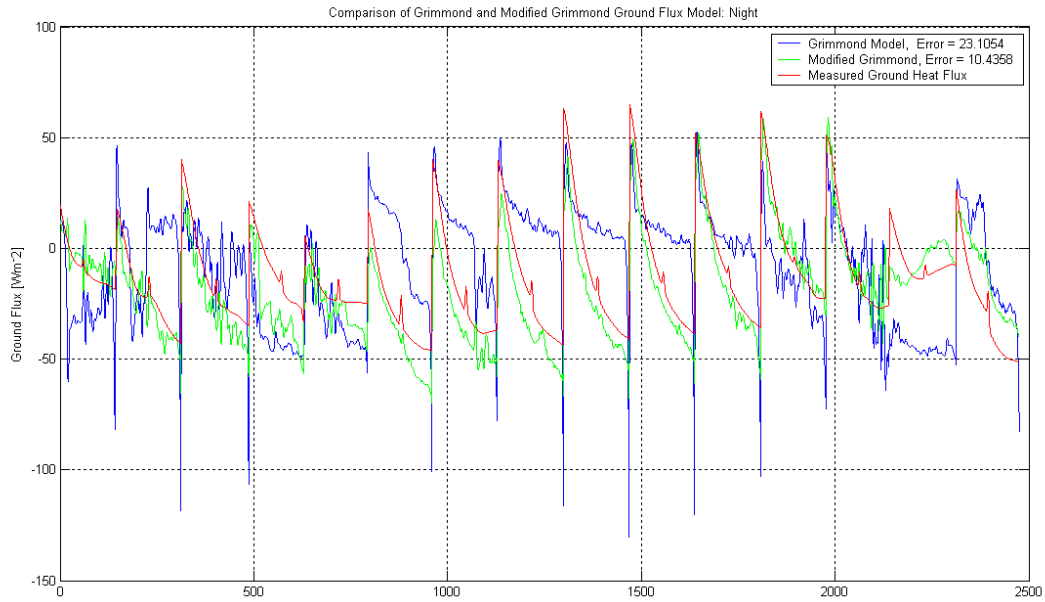


Figure 5.16: General Nighttime Ground Models

5.2.2 1 Hour Averages: Citrus Data

Table 5.9 and 5.10 include the regression coefficients of the Grimmund and modified Grimmund ground model. Table 5.11 includes the errors and R^2 values of the two models. Figures 5.17-20 display ground flux models.

Table 5.9: Coefficients of Grimmund Ground Model

	Clear Day	Cloudy Day	Day	Night
a'_1	-0.018852	-0.025899	-0.021467	-1.2581
a'_2	-0.28369	-0.13977	-0.29282	-0.18392
a'_3	9.7724	5.0259	10.9904	-42.6155

Table 5.10: Coefficients of Modified Grimmund Ground Model

	Clear Day	Cloudy Day	Day	Night
a_1	0.015516	0.10351	0.045311	0.77339
a_2	-0.34318	-1.0585	-0.57506	-5.1533
a_3	-0.3224	-0.41416	-0.43019	-0.56692

a_4	0.47149	0.7779	0.58136	1.2662
a_5	0.036328	0.0043183	0.0019823	0.31971
a_6	-0.5008	-0.082424	-0.42226	-1.4975
a_7	-0.88106	-0.36506	-0.75126	0.38645
a_8	0.17321	-0.070315	0.17752	-0.42257
a_9	-56.5185	-134.5221	-58.2537	-262.5542

Table 5.11: R^2 values and Error for Grimmond Ground model and modified version

	Modified Grimmond, Error, Wm^{-2}	Grimmond, Error, Wm^{-2}	Modified Grimmond, R^2	Grimmond, R^2
Clear Day	8.6639	6.0491	0.93425	0.84957
Cloudy Day	11.6506	12.6849	0.91195	0.45615
Day	11.9776	12.9544	0.94347	0.86843
Night	7.8304	18.7264	0.93062	0.36197

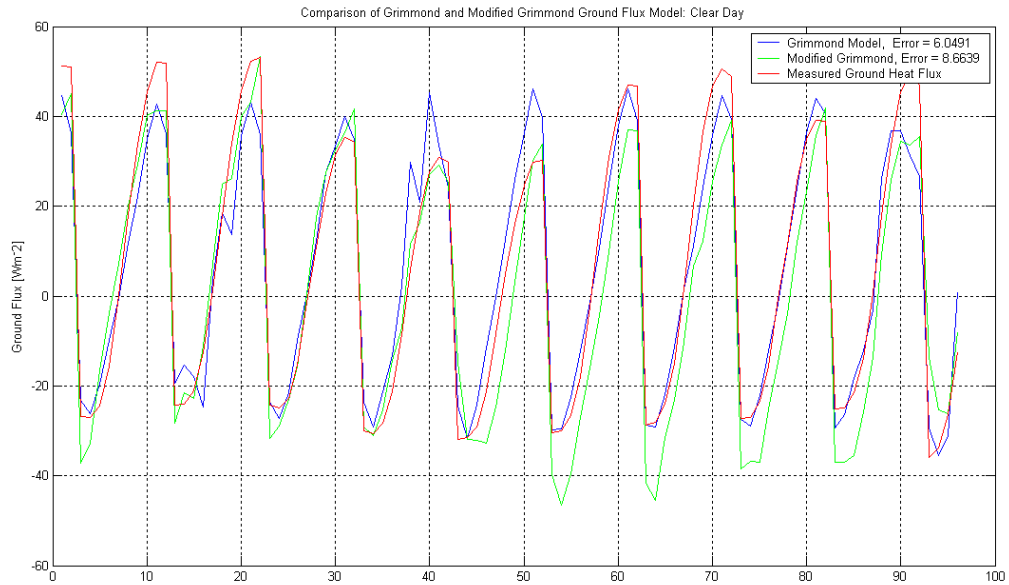


Figure 5.17: Clear Day Ground Model (1-hr average)

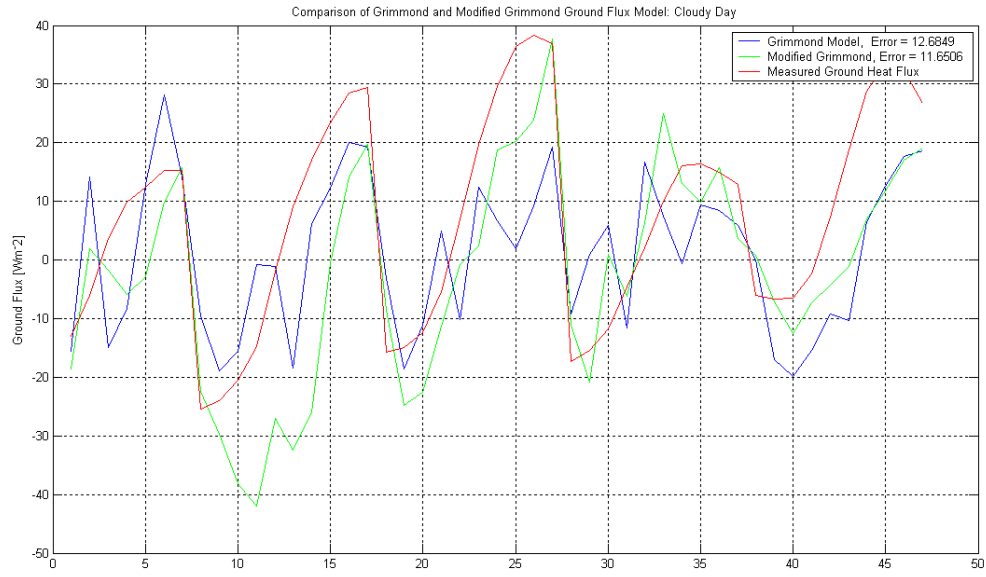


Figure 5.18: Cloudy Day Ground Model (1-hr average)

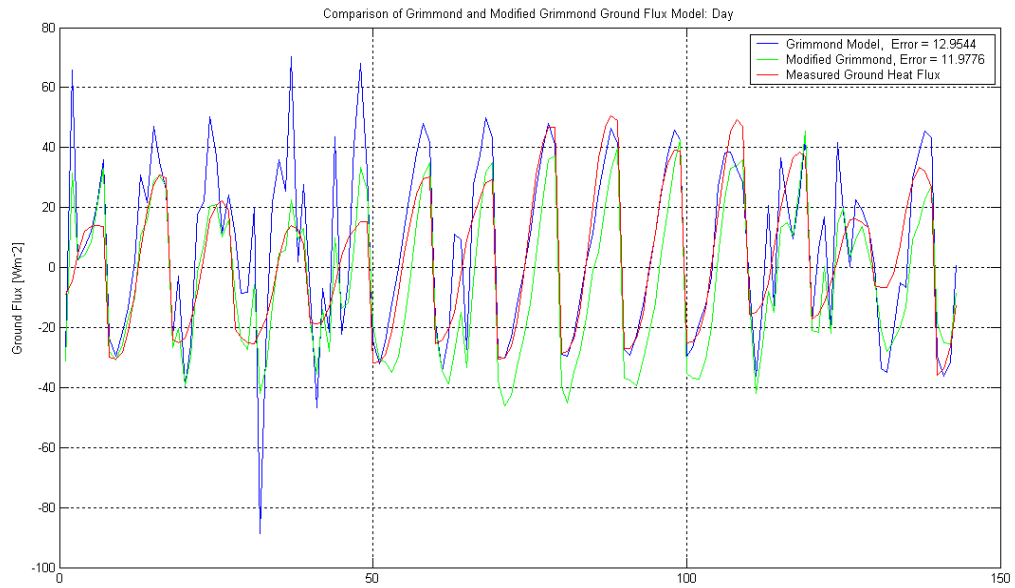


Figure 5.19: Daytime Ground Model (1-hr average)

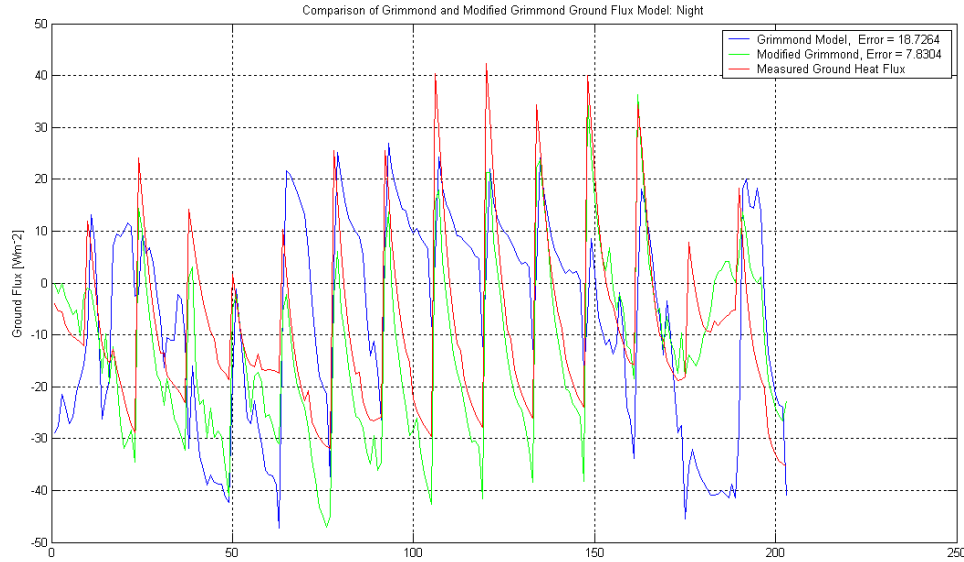


Figure 5.20: Nighttime Ground Model (1-hr average)

5.3 Citrus Site vs. CE-CERT Site

The following ratio analysis illustrates the differences between the Citrus Grove (CG) and CE-CERT (CC) ground surfaces. During clear day, cloudy day, and general daytime condition the ratio of sensible heat to net radiation is larger at the CC site than the CG site. Since net radiation is the major driving component for the surface balance and there is a strong correlation between sensible heat and net radiation, the disparity between the ratios of sensible heat to net radiation must be due to a third element. The source of this addition element is the difference in surface properties between the two sites and the subsequent difference in surface albedo (ratio of outgoing to incoming radiation), Equation 5.10, and ground emmisivity, Equation 5.11. The concrete surface at the CC site reflects less incoming radiation than the CG surface. The radiation that is not reflected is stored in the CC ground where it eventually exits the surface, adding to the pre-existing sensible heat flux due to advection. These results reinforce the fact that

replacing the natural environment with buildings and concrete increases ambient temperature creating the urban heat island effect. Unfortunately instrument malfunction at the CE-CERT site resulted in corrupted latent heat flux measurements.

$$\alpha_s = \frac{Q_{out}}{Q_{in}} \quad (5.10)$$

Table 5.12: Citrus Data Averages

	Clear Day	Cloudy Day	Day	Night
Bowen	-0.4765	3.6540	0.8484	-0.9311
Sensible/Net Radiation	0.2290	-0.3783	0.0248	0.7734
Latent/Net Radiation	0.3662	1.9701	0.9054	-3.5268
Ground/Net Radiation	-0.1146	-2.2864	-0.8446	1.1492
Sensible	68.7951	56.1656	64.5496	-9.0009
Net Radiation	242.7486	188.8480	224.6295	-30.4051
Latent	38.4577	40.8934	39.2764	8.2679
Ground	7.0979	4.0950	6.0884	-5.8007
% Sensible	17.2614	18.0241	17.5178	15.0281
% Net Radiation	60.4485	53.1760	58.0038	46.3806
% Latent	10.8659	17.2450	13.0103	13.2748
% Ground	11.4241	11.5549	11.4681	25.3164
Albedo	0.2004	0.2028	0.2012	N/A

Table 5.13: CE-CERT Data Averages

	Clear Day	Cloudy Day	Day	Night
Bowen	13.6378	-1.6116	11.3646	6.5305
Sensible/Net Radiation	0.6464	0.6660	0.6510	0.5668
Sensible	141.1785	80.1897	126.7683	-26.8589
Net Radiation	366.4933	233.0830	334.9717	-60.2406
Albedo	0.1652	0.1748	0.1675	N/A

6.0 Conclusions

Applying established regression models by other authors showed the need for an improvement. A regression analysis using the components of net radiation and the gradients of these components vastly improves the predictability of the sensible, latent, and ground flux. The gradient approach, originally applied solely to the ground flux can

also be applied to the other terms of the energy balance. This approach is a better model than Grimmond's Ground Model and the Penman-Monteith method. Differences in surface types of the two sites are apparent in the ratios of energy components at the two sites. The lower ground albedo at the CE-CERT site (Tables 5.12 and 5.13) translates to a higher absorption of incoming short wave radiation. The absorbed short wave radiation heats the surface, increasing the ambient temperature of the area. This phenomenon is also shown by the higher ratio of sensible heat to net radiation at the CE-Cert site. These results uphold the fact that urbanization of the natural environment increases ambient temperatures contributing to the urban heat island effect.

There are limitations of my presented model. The model input is the four components of net radiation according to the net radiometer. The availability of all four components depends on the type of radiometer so the model is not applicable for all applications. Also, my model includes many more terms than the other models discussed making it more complex and susceptible to error.

Appendix A: Instrumentation

The first stage of the experiment involved the setup of instruments at the UC Riverside Citrus Grove. The grove is adjacent to the main campus and serves as a site for extensive research of citrus variety fruits. With the permission of Dr. Thomas Ortega at the Citrus Grove we setup instruments on a pre-existing tower in the southwest corner of the fields. The following instruments were deployed to measure the components of the energy balance at the surface of the earth: Ground water reflectometer, soil heat flux plate, sonic anemometer, krypton hygrometer, net radiometer, relative humidity probe,

infrared temperature sensor, data logger, and solar panels. Some of these instruments work together and others independent of each other to calculate the constituents of the energy balance. Basic information of each instrument is given in the following subsections.

A.1 Water Content Reflectometer

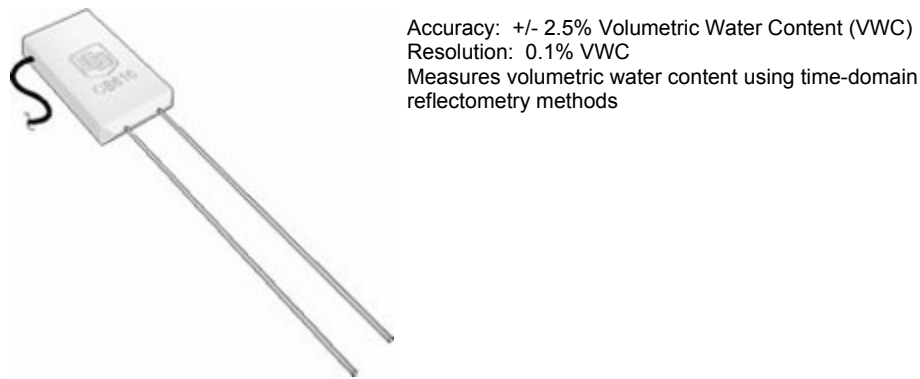


Figure A.1: Picture of soil water content reflectometer with accuracy, resolution, and basic operating principle

The water content reflectometer (Figure A.1) is used to measure water content of the soil which is used to estimate the soil heat capacity needed for calculation of the energy stored in the ground. It makes measurements based on the dielectric permittivity of the soil. Compared to the other constituents of soil, water has the highest dielectric permittivity and is the only component other than air that changes in concentration. Therefore, the water content reflectometer measures soil water content indirectly by its sensitivity to the dielectric permittivity of the material surrounding the probe rods. The probe operates by propagating an electromagnetic pulse along the probe rods at a velocity that is dependent on the dielectric permittivity of the soil surrounding the probe. As water content increases, the propagation velocity decreases. This slowing is due to the

electro-magnetic wave slowing as it polarizes an increasing number of water molecules. The travel time of the applied signal along 2 times the rod length is measured since the applied signal travels the length of the probe rods and reflects from the rod ends back to the probe head. When the reflection is detected the next pulse is triggered. The frequency of this pulsing in free air is about 70 MHz. Therefore, changes in this frequency are directly related to the water content of the soil. The probe output period is empirically related to water content using the following equation:

$$\%VWC = C_o + C_1 t + C_2 t^2 \quad (A.1)$$

where t is travel time in microseconds, $C_o = -0.0663$, $C_1 = -0.0063(\mu s)^{-1}$, and $C_2 = 0.0007(\mu s)^{-2}$.

A.2 HFP01SC Soil Heat Flux Plate



Measurement Range: ± 100
Accuracy: $\pm 3\%$ of reading
Nominal Signal Range: ± 5 mV
Sensitivity: 67

Figure A.2: Picture of soil heat flux plate with measurement range, accuracy, nominal signal range, and sensitivity

The heat flux at the soil surface is made up of two quantities. The first is the heat flux through the plate which is measured by the heat flux plate (Figure A.2) located at a certain depth in the soil. The second quantity is the amount of energy stored in the ground between the heat flux plate and the surface. Four evenly spaced averaging soil thermocouples measure temporal changes in the temperature of the soil layer above the heat flux plate. See Figure A.3. for the schematic.

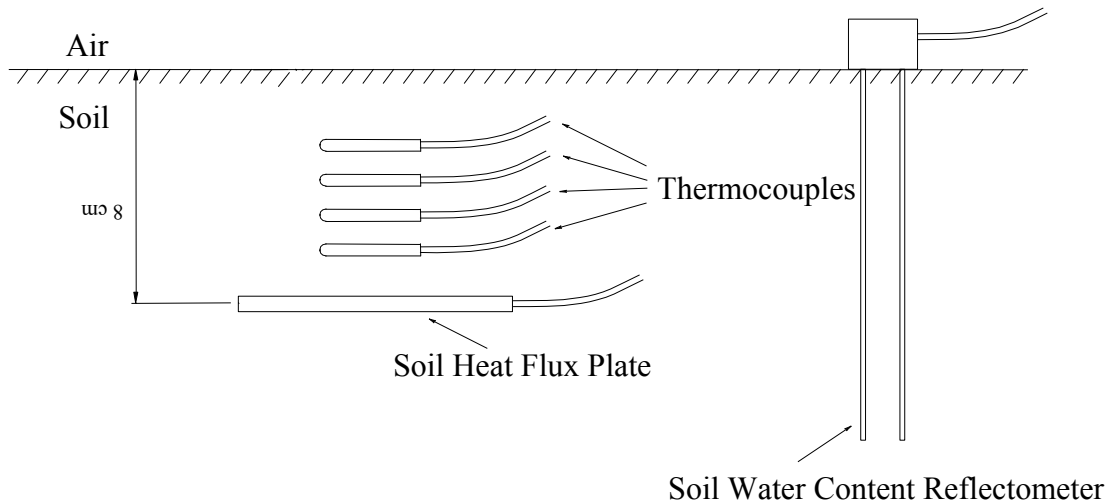


Figure A.3: Schematic of soil heat flux plate, thermocouples and soil water content reflectometer.

The average soil temperature is calculated by first taking the average of the top two and bottom two thermocouples. Then these two averages are combined to make the average soil temperature, ΔT_s . This average temperature and measurements from the soil water content reflectometer are used to calculate the ground storage term. Additional quantities, such as the heat capacity of the soil and specific heat of the dry soil are needed to find the flux at the surface. The bulk heat capacity of the soil is calculated by adding the specific heat of the dry soil to that of the soil water. The values used for specific heat of dry soil and water on a mass basis. The heat capacity of the moist soil is:

$$c_s = \rho_b [X_b c_d + (1 - X_b) c_w] \theta_m = \frac{\rho_w}{\rho_b} \theta_v c_w \quad (A.2)$$

where c_s is the heat capacity of moist soil, ρ_b is the bulk density, ρ_w is the density of water, c_d is the heat capacity of a dry mineral soil (approximated as $840 \text{ J kg}^{-1} \text{ K}^{-1}$ according to instrument manual), θ_m is soil water content on a mass basis, θ_v is soil water content on a volume basis, and c_{ows} is the heat capacity of water. Finally, the storage term and soil heat flux at the surface are:

$$S = \frac{\Delta T_s c_s d}{t} \quad (A.3)$$

$$G_{surface} = G_{plate} + S \quad (A.4)$$

where d is the depth of the flux plate, G_{plate} is the flux measured by the heat flux plate, and $1/t$ is the frequency of measurement.

A.3 CSAT3 Sonic Anemometer



Measurement Rate: 1 to 60 Hz
Error due to noise: 1 (x and y-direction)
0.5 (z-direction)



Figure A.4: Picture of sonic anemometer with measurement rate and error due to noise

The sonic anemometer (Figure A.4) measures three wind components and temperature at a very fast sampling rate. The instrument head consists of three non-orthogonal pairs of the ultra sonic transducers. Each axis, pair of transducers, of the anemometer pulses two ultrasonic signals in opposite directions and measures the travel time. The travel time of the first signal (out) is:

$$t_o = \frac{d}{c + u_a} \quad (\text{A.5})$$

and the travel time of the second signal (back) is:

$$t_b = \frac{d}{c - u_a} \quad (\text{A.6})$$

where u_a is the wind speed along any transducer axis, d is the distance between the transducers, and c is the speed of sound. The wind speed, u_a along any axis can be found from (A.5) and (A.6) as

$$u_a = \frac{d}{2} \left[\frac{1}{t_o} - \frac{1}{t_b} \right] \quad (\text{A.7})$$

The wind speed on all three non-orthogonal axis are given by u_a , u_b , and u_c , where indices a , b , and c refer to the non-orthogonal sonic axes. These velocity vectors are decomposed into orthogonal axes by the following transformation:

$$\begin{bmatrix} u_x \\ u_y \\ u_z \end{bmatrix} = A \begin{bmatrix} u_a \\ u_b \\ u_c \end{bmatrix}, \quad (\text{A.8})$$

where matrix A is a 3x3 coordinate transformation matrix that is unique to each CSAT3 and it is stored in ROM memory. Further, the speed of sound can also be calculated and used for the temperature measurements. The anemometer is able to determine the speed of sound via (A.5) and (A.6) as

$$c = \frac{d}{2} \left[\frac{1}{t_o} + \frac{1}{t_b} \right]. \quad (\text{A.9})$$

Also, the specific heats for moist air at constant pressure and volume, according to the user's manual, are given by:

$$c_p = qc_{pw} + (1 + q)c_{pd} = c_{pd}(1 + 0.84q) \quad (\text{A.10})$$

$$c_v = qc_{vw} + (1 + q)c_{vd} = c_{vd}(1 + 0.93q) \quad (\text{A.11})$$

where c_p and c_v are the specific heats of moist air at constant volume and pressure, c_{pw} and c_{vw} is the specific heat of water vapor, c_{pd} and c_{vd} is the specific heat of dry air, respectively. Taking the equations of c_p and c_v and plugging into Equation A.12 gives Equation 2.15.

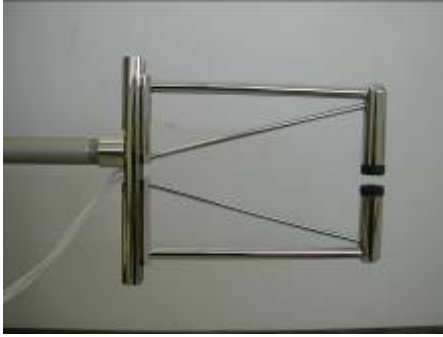
$$c^2 = \frac{\gamma P}{\rho} = \gamma R_d T_v = \gamma R_d T(1 + 0.61q) \quad (\text{A.12})$$

Finally, the sonic temperature, in degrees Celsius, is given by the following equation:

$$T_s = \frac{c^2}{\gamma_d R_d} - 273.15 \quad (\text{A.13})$$

where $\gamma_d = 1.4$ and $R_d = 287.04 \text{ JK}^{-1}\text{kg}^{-1}$. Once the air temperature and wind velocity in the vertical direction are found, the sensible heat flux according to the eddy covariance formulation is calculated according to Equation 2.9

A.4 KH20 Krypton Hygrometer



Measures rapid fluctuations in atmospheric water vapor
Max Frequency Response: 100 Hz



Figure A.5: Picture of krypton hygrometer with max frequency response

The atmospheric water vapor measurements of the hygrometer (Figure A.5) and the velocity fluctuation measurements by the anemometer form the basis for the calculation of the latent heat flux. The hygrometer contains a lamp that emits light at both 123.58 and 116.49 nm. Both of these wavelengths are absorbed by water vapor and oxygen. The hygrometer signal in terms of the absorption of both wavelengths by water vapor and oxygen according to the instrument user manual is:

$$V_h = V_{o1} \exp(-xk_{w1}\rho_v - xk_{o1}\rho_o) + V_{o2} \exp(-xk_{w2}\rho_v - xk_{o2}\rho_o) \quad (\text{A.14})$$

Where V_h is the signal voltage from the hygrometer, V_{o1} and V_{o2} are the signals with no absorption of each wavelength, x is the path length of the hygrometer, k_{w1} and k_{w2} are the absorption coefficients for water vapor of each wavelength, k_{o1} and k_{o2} are the absorption coefficients for oxygen, and finally ρ_v and ρ_o are the densities of water vapor and oxygen. If $V_{o1} \gg V_{o2}$ and $k_{w1} \sim k_{w2}$ Equation A.14 can be rewritten by approximating the individual absorption of the two wavelengths and replacing them with a single effective coefficient for either water vapor or oxygen. Combining water absorption coefficients gives:

$$V_h = V_{o1} \exp(-xk_w\rho_v)[\exp(-xk_{o1}\rho_o) + (V_{o2}/V_{o1})\exp(-xk_{o2}\rho_o)] \quad (\text{A.15})$$

Now, combining the oxygen absorption coefficients gives:

$$V_h = V_{o1} \exp(-xk_w\rho_v)[\exp(-xk_o\rho_o) + (V_{o2}/V_{o1})\exp(-xk_o\rho_o)] \quad (\text{A.16})$$

Since in practice $V_{o1} \gg V_{o2}$, $(V_{o2}/V_{o1}) \rightarrow 0$ and Equation A.18 reduces to:

$$V_h = V_o \exp(-xk_w\rho_v) \exp(-xk_o\rho_o) \quad (\text{A.17})$$

Taking the natural log of Equation A.17 and solving for ρ_v gives:

$$\rho_v = \frac{\ln V_h}{-xk_w} - \frac{\ln V_o}{-xk_w} + \frac{k_o}{-k_w} \rho_o \quad (\text{A.18})$$

The Reynolds decomposition of the covariance of the vertical wind speed and water vapor is:

$$\overline{w'\rho'_v} = \overline{w\rho_v} - \overline{w\rho_v} \quad (\text{A.19})$$

Substituting Equation A.18 into A.19 gives:

$$\overline{w'\rho'_v} = \frac{\overline{w(\ln V_h)} - \overline{w} \overline{\ln V_h}}{-xk_w} + \frac{k_o}{-k_w} (\overline{w\rho_o} - \overline{w\rho_o}) \quad (\text{A.20})$$

The first term in Equation A.20 is the water vapor flux and the other is the oxygen correction. The density of oxygen is not directly measured but can be written in terms of measured variables using the ideal gas law:

$$\rho_o = \frac{PC_oM_o}{RT} \quad (\text{A.21})$$

where P is atmospheric pressure, T is air temperature, C_o is the concentration of oxygen, M_o is the molecular weight of oxygen, and R is the universal gas constant. Substituting Equation A.21 into Equation A.20 gives

$$\overline{w'\rho_v'} = \frac{\overline{w(\ln V_h)} - \bar{w} \overline{\ln V_h}}{-xk_w} + \frac{k_o}{-k_w} \frac{PC_oM_o}{R} \left[\overline{wT^{-1}} - \bar{w} \overline{T^{-1}} \right] \quad (\text{A.22})$$

Finally, applying a “reverse” Reynolds decomposition to the numerator of the first term and the quantity in the brackets gives the latent heat flux:

$$LE = \lambda \frac{\overline{w'(\ln V_h)'}}{-xk_w} + OC_1 \quad (\text{A.23})$$

where OC_1 is:

$$OC_1 = \lambda \frac{k_o}{-k_w} \frac{PC_oM_o}{R} \overline{w'(T^{-1})'} \quad (\text{A.24})$$

A.5 CNR1 Net Radiometer



Measurement Range: -250 to 250 [0 to 15 mili-V]
Spectral Range: 305 to 2800 nm
Sensitivity: 10 to 35 microVolts/(
Expected error for daily sum: +/- 10%



Figure A.6: Picture of net radiometer with measurement range, spectral range, sensitivity, and expected daily error

The net radiometer (Figure A.6) measures the net radiation at the earth's surface independent of the other instruments in the system. Its design is such that the upward and downward facing instruments on the radiometer, receive radiation from the entire hemispherical field of view above and below the instrument. The total spectral range that is measured is from 0.3 to 50 micrometers. Specifically, the radiometer measures net short wave solar radiation (0.3 to 3 micrometers) using two CM3 pyranometers. Net short wave radiation is simply calculated by taking the difference between the irradiance measurements of the upper and lower pyranometers:

$$\text{Net Solar radiation} = (E \text{ upper CM3}) - (E \text{ lower CM3}) \quad (\text{A.25})$$

Similarly, calculating the net far infrared radiation (5 to 50 micrometers) is the difference between the upper and lower CG3 pyrgeometers irradiance measurements:

$$\text{Net Far Infrared radiation} = (E \text{ upper CG3}) - (E \text{ lower CG3}) \quad (\text{A.26})$$

The CM3 pyranometer generates a voltage (millivolts) signal that is proportional to the incoming solar radiation:

$$E = \frac{V}{C} \quad (\text{A.27})$$

Solar irradiance E , is a function of voltage V , and calibration constant C . But, operation of the CG3 pyrgeometer is a bit more complicated. The signal generated by the CG3 represents the exchange of far infrared radiation between the instrument and the object it's facing. The directionality of this exchange is reflected in the sign of the output voltage. When the object the instrument is facing is warmer than its own sensor housing, the output voltage will be positive. When the object is colder the signal will be negative. Therefore the temperature of the instrument housing must be taken into consideration when measuring radiation. A Pt-100 thermocouple is attached to the CG3, within the CNR1's housing. Far infrared irradiance, E , according to the instrument user manual is given by

$$E = \frac{V}{C} + 5.67 \times 10^{-8} * T^4, \quad (\text{A.28})$$

where C is the sensitivity of the sensor, and T is the housing temperature in Kelvin.

A.6 HMP45-C Relative Humidity Probe



Relative Humidity Measurement Range: 0 to 100%
Accuracy: +/- 2% RH (0 to 90% relative humidity)
 +/- 3% RH (90 to 100% relative humidity)
Temperature Measurement Range: -40 °C to +60 °C
Temperature Measurement Accuracy: +/- 0.4 °C

Figure A.7: Picture of relative humidity probe with humidity measurement range, humidity accuracy, temperature measurement range, and temperature measurement accuracy

The HMP45C Temperature and Relative Humidity (Figure A.7) probe contains a Pt Resistance Temperature detector (PRT) and a Vaisala HUMICAP 180 capacitive relative humidity sensor. The probe outputs relative humidity defined as:

$$RH = \frac{e}{e_s} * 100 \quad (A.29)$$

where RH is the relative humidity, e is the vapor pressure in kPa, and e_s is the saturation vapor pressure in kPa. Vapor pressure is an absolute measure of the amount of water vapor in air and is a function of the dew point temperature. The dew point temperature is the temperature to which the air must be cooled for water vapor to reach saturation. The saturation vapor pressure is the maximum amount of water vapor that air can hold at a given temperature. When air temperature increases the saturation vapor pressure also increases. Conversely, a decrease in air temperature causes a decrease in saturation vapor pressure. Therefore, according to Equation A.29 a change in air temperature will change the relative humidity without changing the absolute humidity (The amount of water vapor present in a unit volume of air). After an increase in air temperature, air can hold more

water vapor. But, the actual amount of water vapor in the air has not changed. As a result, the amount of water vapor in the air, relative to saturation, has decreased. For this reason, relative humidity is calculated by measuring the mean vapor pressure and saturation vapor pressure.

A.7 IRTS-P Infrared Temperature Sensor



Measurement range: -10 to 55 deg C
Accuracy: +/- 0.3 deg C from -10 to 55 deg C
Response Time: less than 1 second to changes in target temperature

Figure A.8: Picture of infrared temperature sensor with measurement range, accuracy, and response time

Since the infrared temperature sensor (Figure A.8) is a non-contact means of measuring the surface temperature of an object, it is an ideal tool for measuring the surface temperature of the earth. Detecting temperature by sensing infrared radiation avoids the problems of influencing the temperature by contact and maintaining thermal contact, while providing a good spatial average. The sensor is calibrated to output the signal for the target temperature with the same output voltage as a K-Type thermocouple measuring the same target. A separate K-type thermocouple is used to measure the temperature of the sensor body to correct target temperature readings for greater accuracy. The field of view of the sensor is based on the geometry of both the sensor and lens. Atmospheric scattering and unwanted reflections from outside the field of view negatively influence the measurement. Usually, 80 to 90% of the signal is from the field of view with the remaining coming from the surrounding field of view. The corrected

target temperature (CTT) is calculated as a difference between the apparent target temperature (ATT) and the sensor error correction (SER) (Bugbee et. al. 1996). The sensor error correction is calculated as

$$SEC = \left[\frac{0.25}{P_{sb}} \right] \left[(ATT - H_{sb})^2 - K_{sb} \right] \quad (A.30)$$

where

$$\begin{aligned} P_{sb} &= 49.9092 + 0.59237 * sb + 0.00558 * sb^2 \\ H_{sb} &= 4.2828 + 0.4248 * sb - 0.00077 * sb^2 \\ K_{sb} &= 52.0705 - 5.3826 * sb + 0.387 * sb^2 \end{aligned} \quad (A.31-A.34)$$

with sb being the surface body temperature.

A.8 CR 5000 DataLogger



Programmed using LoggerNet or
PC9000 Support Software for
Windows
PC Card: Types I, II, III

Figure A.9: Picture of CR5000 datalogger

The wires from all of the instruments go to the datalogger (Figure A.9). There are 20 differential or 40 single-ended inputs for measuring voltages up to +/- 5V. The logger also includes a heavy copper grounding bar and connectors. This along with the design of the case, according to the manufacturer, reduces temperature gradients for accurate thermocouple measurements. Signal resolution on the most sensitive range is 0.67 μ V. There are 8 digital I/O channels (0V low, 5V high) for frequency measurement, digital

control, and triggering. Measurements taken from the instruments of our system are processed by the datalogger and stored on a PCMCIA card in table form. The logger has a slot for a Type 1/2/3 PCMCIA card. A keyboard display is used to check card status and to power the card down before removal. Removing the card while it's active will cause garbled data and can actually damage the card.

The CR5000 has two power operation modes. The low profile mode without any power supply requires an external DC power source connected to the Power In terminal on the panel. The lead acid battery power supply mode includes a 7 amp hour battery with built in charging regulator and includes an AC adapter for use where 120 VAC is available. Charging power can also come from a 17-28 VDC input from a solar panel. We use a combination of the two modes with a 12 VDC car battery connected to the Power In terminal and a BP solar panel is connected to the charging regulator.

The datalogger has a 2MB SRAM and 1 MB Flash EEPROM memory. The operating system and user programs are stored in flash EEPROM memory. The memory that is not used by the operating system and program are available for data storage which can be used to store data in the time between when the card is removed and re-inserted. We are only losing 2 to 3 data points in the time it takes to extract data from the card. The datalogger divides a program into two tasks. The measurement task manipulates the measurement and control hardware on a rigidly times sequence. The second task, the processing task, processes and stores the resulting measurements. The measurement task stores raw Analog to Digital Converter (ADC) data directly into memory. As soon as the data from an instrument scan is in memory, the processing task starts. There are two

buffers allocated for the raw ADC data, so one buffer can be used to process data while the other used to fulfill the measurement task.

Appendix B: Statistical Analysis

B.1 Correlation and Covariance

The sensible and latent heat fluxes are calculated according to the eddy covariance theory. The main assumption is that there is a strong correlation between the fluctuation of the vertical component of velocity, w' (with respect to the surface of the earth) and the fluctuation of a measurable quantity, *e.g.* p' . The flux of P passing through the plane perpendicular to the vertical velocity component can then be expressed as a factor of this correlation (Denmead, 1996):

$$\text{Flux of } p \propto bc \cdot \overline{w'p'} \quad (\text{B.1})$$

Constants b and c are such that the overall units of the flux are W/m^2 . Covariance and correlation are related parameters that indicate the extent to which two random variables co-vary. Parameters that co-vary increase and decrease together and covariance and correlation measure this tendency. Consider random vectors X_i and Y_i of length n :

$$X_i = \begin{pmatrix} X_1 \\ X_2 \\ \vdots \\ X_n \end{pmatrix}, Y_i = \begin{pmatrix} Y_1 \\ Y_2 \\ \vdots \\ Y_n \end{pmatrix} \quad (\text{B.2})$$

Given any pair of components, X_i and Y_i their covariance is written as $\text{cov}(X_i, Y_i)$ or

Σ_{xy} and defined by the equation:

$$\text{cov}(X_i, Y_i) = \overline{(X_i - \mu_x)(Y_i - \mu_y)} \quad (\text{B.3})$$

Where μ_x and μ_y are the means of X_i and Y_i . By definition, the resulting covariance matrix is symmetric, with $\Sigma_{xy} = \Sigma_{yx}$. Also, the covariance of any component X_i with itself is that component's variance:

$$\text{cov}(X_i, X_i) = \overline{(X_i - \mu_x)^2} = \text{var}(X_i) \quad (\text{B.4})$$

Considering all combinations of covariance between elements of vectors X_i and Y_i , gives the covariance matrix:

$$\Sigma_{xy} = \begin{pmatrix} \Sigma_{11} & L & \Sigma_{1n} \\ M & 0 & M \\ \Sigma_{n1} & L & \Sigma_{nn} \end{pmatrix} \quad (\text{B.5})$$

The magnitude of covariance Σ_{xy} depends upon the standard deviations of X_i and Y_i . To obtain a more direct indication of how two components co-vary, the covariance is scaled to obtain what is known as a correlation. Given X_i and Y_i their correlation is written as $\text{cor}(X_i, Y_i)$ or ρ_{xy} and is defined as:

$$\rho_{xy} = \frac{\text{cov}(X_i, Y_i)}{\sigma_x \sigma_y} \quad (\text{B.6})$$

where σ_x and σ_y are the standard deviations of X_i and Y_i . Not only is the correlation calculation key to heat flux measurements, it is also used in the linear regression analysis of the data.

B.2 Regression Analysis

A regression analysis is used to model the constituents of the energy balance. Time dependency is eliminated by modeling the constituents as a function of the four

components of net radiation. And, the many statistical parameters resulting from a regression analysis give an accurate means of measuring how well the model fits the data. The basic form of the regression analysis is used to model simple curves while more complicated forms of the regression are used to model more complicated curves. Statistical/mathematical restrictions on the independent variable(s) of the various types of regression modes provide a good guide for what the final form of the model will be.

The basic premise of the regression analysis is finding the best-fitting curve to a given set of points by minimizing the sum of the squares of the offsets of the points from a given curve. The sum of the squares of the offsets is used instead of the offset absolute values because this allows the error to be treated as a continuous differentiable quantity. In any minimization problem a derivative will be taken, so it is necessary for the error to be a continuous differentiable quantity. The downside of this squaring is that outliers are magnified greatly and can have a significant negative impact on the model. But, basic filtering techniques can be used to eliminate any outliers.

The error of fit is described as the vertical distance between points and the curve. These values are minimized as opposed to perpendicular offsets. Using vertical offsets provides a fitting function for the independent variable X that estimates y for a given x , allows uncertainties of the data points along the x - and y -axes to be incorporated simply. The linear least squares fitting technique is the simplest and most commonly applied form of linear regression and provides a solution to the problem of finding the best fitting straight line through a set of points. If the relationship between the independent and dependent variables is known to within additive or multiplicative constants, it is common

practice to transform the data so that a plot of the data resembles a line. Table B.1 shows the transformations of a few non-linear functions.

Table B.1: Axis Transformations Used to Linearized Non-Linear Functions

Function	X	Y	y-intercept	Slope
$y = a_1 e^{b_1 x}$	x	$\ln(y)$	$\ln(a_1)$	b_1
$y = a_2 x^{b_2}$	$\log(x)$	$\log(y)$	$\log(a_2)$	b_2
$y = a_3 \frac{x}{b_3 + x}$	$\frac{1}{x}$	$\frac{1}{y}$	$\frac{1}{a_3}$	$\frac{b_3}{a_3}$

This method is one way to maximize the effectiveness of a linear regression but is not used in my analysis. Making such a transformation eventually requires a transformation back to the original axes which is an unnecessary considering the strong linear correlation between net radiation and other terms of the energy balance.

B.2.1 Linear Regression

A linear least squares fitting begins with first finding the sum of the squares of the vertical deviations S_r of a set of n data points from a function f as.

$$S_r^2 = \sum [y_i - f(x_i, a_1, a_2, \dots, a_n)]^2 \quad (\text{B.7})$$

As mentioned earlier the differences are squared to remove any discontinuous derivatives which cannot be treated analytically. The square deviations from each point are therefore summed, and the resulting residual is then minimized to find the best fit line. The condition for S_r^2 to be a minimum is:

$$\frac{\partial (S_r^2)}{\partial a_i} = 0 \quad (\text{B.8})$$

for $i = 1, K, n$. For a linear fit

$$f(a, b) = a + bx \quad (\text{B.9})$$

$$S_r^2(a, b) = \sum_{i=1}^n \left[y_i - (a + bx_i) \right]^2 \quad (\text{B.10})$$

The minimization is carried out by taking the derivative of Equation 10 with respect to first b then a :

$$\frac{\partial (S_r^2)}{\partial b} = -2 \sum_{i=1}^n \left[y_i - (a + bx_i) \right] x_i = 0 \quad (\text{B.11})$$

$$\frac{\partial (S_r^2)}{\partial a} = -2 \sum_{i=1}^n \left[y_i - (a + bx_i) \right] = 0 \quad (\text{B.12})$$

Distributing the sum over each of the terms in both Equation 11 and 12 leads to the equations:

$$na + b \sum_{i=1}^n x_i = \sum_{i=1}^n y_i \quad (\text{B.13})$$

$$a \sum_{i=1}^n x_i + b \sum_{i=1}^n x_i^2 = \sum_{i=1}^n x_i y_i \quad (\text{B.14})$$

Rewriting the pair of equations in matrix form gives:

$$\begin{bmatrix} n & \sum_{i=1}^n x_i \\ \sum_{i=1}^n x_i & \sum_{i=1}^n x_i^2 \end{bmatrix} \begin{bmatrix} a \\ b \end{bmatrix} = \begin{bmatrix} \sum_{i=1}^n y_i \\ \sum_{i=1}^n x_i y_i \end{bmatrix} \quad (\text{B.15})$$

$$\begin{bmatrix} a \\ b \end{bmatrix} = \begin{bmatrix} n & \sum_{i=1}^n x_i \\ \sum_{i=1}^n x_i & \sum_{i=1}^n x_i^2 \end{bmatrix}^{-1} \begin{bmatrix} \sum_{i=1}^n y_i \\ \sum_{i=1}^n x_i y_i \end{bmatrix} \quad (\text{B.16})$$

The 2x2 matrix inverse is

$$\begin{bmatrix} a \\ b \end{bmatrix} = \frac{1}{n \sum_{i=1}^n x_i^2 - \left(\sum_{i=1}^n x_i \right)^2} \begin{bmatrix} \sum_{i=1}^n y_i \sum_{i=1}^n x_i^2 - \sum_{i=1}^n x_i \sum_{i=1}^n x_i y_i \\ n \sum_{i=1}^n x_i y_i - \sum_{i=1}^n y_i \sum_{i=1}^n x_i \end{bmatrix} \quad (\text{B.17})$$

Therefore coefficients a and b are:

$$a = \frac{\sum_{i=1}^n y_i \sum_{i=1}^n x_i^2 - \sum_{i=1}^n x_i \sum_{i=1}^n x_i y_i}{n \sum_{i=1}^n x_i^2 - \left(\sum_{i=1}^n x_i \right)^2} = \frac{\bar{y} \left(\sum_{i=1}^n x_i^2 \right) - \bar{x} \sum_{i=1}^n x_i y_i}{\sum_{i=1}^n x_i^2 - n \bar{x}^2} \quad (\text{B.18})$$

$$b = \frac{n \sum_{i=1}^n x_i y_i - \sum_{i=1}^n x_i \sum_{i=1}^n y_i}{n \sum_{i=1}^n x_i^2 - \left(\sum_{i=1}^n x_i \right)^2} = \frac{\left(\sum_{i=1}^n x_i \sum_{i=1}^n y_i \right) - n \bar{x} \cdot \bar{y}}{\sum_{i=1}^n x_i^2 - n \bar{x}^2} \quad (\text{B.19})$$

These can be rewritten in a simpler form by defining the sums of squares

$$SS_{xx} = \sum_{i=1}^n (x_i - \bar{x})^2 = \left(\sum_{i=1}^n x_i^2 \right) - n \bar{x}^2 \quad (\text{B.20})$$

$$SS_{yy} = \sum_{i=1}^n (y_i - \bar{y})^2 = \left(\sum_{i=1}^n y_i^2 \right) - n \bar{y}^2 \quad (\text{B.21})$$

$$SS_{xy} = \sum_{i=1}^n (x_i - \bar{x})(y_i - \bar{y}) = \left(\sum_{i=1}^n x_i y_i \right) - n \bar{x} \cdot \bar{y} \quad (\text{B.22})$$

which are also written as

$$\sigma_x^2 = \frac{SS_{xx}}{n} \quad (\text{B.23})$$

$$\sigma_y^2 = \frac{SS_{yy}}{n} \quad (\text{B.24})$$

$$\text{cov}(x, y) = \frac{SS_{xy}}{n} \quad (\text{B.25})$$

Here, $\text{cov}(x, y)$ is the covariance and σ_x^2 and σ_y^2 are variances. In terms of the sums of squares, the regression coefficient b is given by

$$b = \frac{\text{cov}(x, y)}{\sigma_x^2} = \frac{SS_{xy}}{SS_{xx}} \quad (\text{B.26})$$

and a is given in terms of b as

$$a = \bar{y} - b\bar{x} \quad (\text{B.27})$$

The overall quality of the fit is then parameterized in terms of the correlation coefficient, defined by

$$r^2 = \frac{SS_{xy}^2}{SS_{xx}SS_{yy}} \quad (\text{B.28})$$

which gives the proportion of SS_{yy} which is accounted for by the regression.

Let \hat{y}_i be the vertical coordinate of the best-fit line with x-coordinate x_i :

$$\hat{y}_i \equiv a + bx_i \quad (\text{B.29})$$

Then, the error between the actual vertical point y_i and the fitted point is given by

$$e_i \equiv y_i - \hat{y}_i = S_r \quad (\text{B.30})$$

Define s^2 as an estimator for the variance in terms of error e_i ,

$$s^2 = \sum_{i=1}^n \frac{e_i^2}{n-2} \quad (\text{B.31})$$

Then s can be given by

$$s = \sqrt{\frac{SS_{yy} - bSS_{xy}}{n-2}} = \sqrt{\frac{SS_{yy} - \frac{SS_{xy}^2}{SS_{xx}}}{n-2}} \quad (\text{B.32})$$

The standard errors for a and b are

$$SE(a) = s \sqrt{\frac{1}{n} + \frac{\bar{x}^2}{SS_{xx}}} \quad (\text{B.33})$$

$$SE(b) = \frac{s}{\sqrt{SS_{xx}}} \quad (\text{B.34})$$

B.2.2 Polynomial Regression

So far a procedure was developed to derive the equation of a straight line using the least-squares criterion. Some engineering data that seems to resemble linear behavior is sometimes poorly represented by a straight line. In this case, a curve or some type of polynomial could better fit the data. As discussed in the previous section, a method to accomplish this is to use transformations but a better method is to fit polynomials to the data using polynomial regression.

Similar to the linear regression, the square deviations from each point of the data from a higher order polynomial are summed and minimized. For example, suppose that a fit is to be made to a second-order polynomial:

$$y = a_o + a_1x + a_2x^2 + e \quad (\text{B.35})$$

The sum of the squares of the error is:

$$S_r = \sum_{i=1}^n \left(y_i - a_o - a_1x_i - a_2x_i^2 \right)^2 \quad (\text{B.36})$$

Following the procedure of the previous section, we take the derivative of Equation B.36 with respect to each of the unknown coefficients of the polynomial:

$$\frac{\partial S_r}{\partial a_o} = -2 \sum_{i=1}^n \left(y_i - a_o - a_1x_i - a_2x_i^2 \right) \quad (\text{B.37})$$

$$\frac{\partial S_r}{\partial a_1} = -2 \sum_{i=1}^n x_i \left(y_i - a_o - a_1x_i - a_2x_i^2 \right) \quad (\text{B.38})$$

$$\frac{\partial S_r}{\partial a_2} = -2 \sum_{i=1}^n x_i^2 \left(y_i - a_o - a_1x_i - a_2x_i^2 \right) \quad (\text{B.39})$$

These equations can be set equal to zero and rearranged to develop the following set of equations:

$$\begin{aligned} (n) a_o + \left(\sum x_i \right) a_1 + \left(\sum x_i^2 \right) a_2 &= \sum y_i \\ \left(\sum x_i \right) a_o + \left(\sum x_i^2 \right) a_1 + \left(\sum x_i^3 \right) a_2 &= \sum x_i y_i, \\ \left(\sum x_i^2 \right) a_o + \left(\sum x_i^3 \right) a_1 + \left(\sum x_i^4 \right) a_2 &= \sum x_i^2 y_i \end{aligned} \quad (\text{B.40-}$$

B.42)

or in matrix form:

$$\begin{bmatrix} n & \sum x_i & \sum x_i^2 \\ \sum x_i & \sum x_i^2 & \sum x_i^3 \\ \sum x_i^2 & \sum x_i^3 & \sum x_i^4 \end{bmatrix} \begin{bmatrix} a_o \\ a_1 \\ a_2 \end{bmatrix} = \begin{bmatrix} \sum y_i \\ \sum x_i y_i \\ \sum x_i^2 y_i \end{bmatrix} \quad (\text{B.43})$$

where all summations are from $i = 1$ through n . The above three equations are linear and have three unknowns a_o , a_1 , and a_2 . For this case, it is apparent that the problem of

determining a least-squares second order polynomial is equivalent to solving a system of three simultaneous linear equations. And, the procedure for this example of a second order polynomial can be easily extended to an m-th order polynomial as

$$y = a_0 + a_1x + a_2x^2 + \dots + a_mx^m + e \quad (\text{B.43})$$

Therefore, determining the coefficients of an m-th order polynomial is equivalent to solving a system of m+1 simultaneous linear equations with the standard error given as:

$$s_{y/x} = \sqrt{\frac{S_r}{n - (m + 1)}} \quad (\text{B.44})$$

B.2.3 Multiple Linear Regression

Another extension of linear regression is the case where y is a linear function of two or more independent variables. For example, y might be a linear function of x_1 and x_2 as in:

$$y = a_0 + a_1x_1 + a_2x_2 + e \quad (\text{B.45})$$

As in the previous cases, the best values of the coefficients are determined by setting up the sum of the squares of the residuals (error),

$$S_r = \sum_{i=1}^n (y_i - a_0 - a_1x_{1i} - a_2x_{2i})^2, \quad (\text{B.46})$$

and differentiating with respect to each of the unknown coefficients gives:

$$\begin{aligned} \frac{\partial S_r}{\partial a_0} &= -2 \sum_{i=1}^n (y_i - a_0 - a_1x_{1i} - a_2x_{2i}) \\ \frac{\partial S_r}{\partial a_1} &= -2 \sum_{i=1}^n x_{1i} (y_i - a_0 - a_1x_{1i} - a_2x_{2i}) \\ \frac{\partial S_r}{\partial a_2} &= -2 \sum_{i=1}^n x_{2i} (y_i - a_0 - a_1x_{1i} - a_2x_{2i}) \end{aligned} \quad (\text{B.47-B.49})$$

The coefficients yielding the minimum sum of the squares of the residuals are obtained by setting the partial derivatives equal to zero and expressing the result in matrix form as:

$$\begin{bmatrix} n & \sum x_{1i} & \sum x_{2i} \\ \sum x_{1i} & \sum x_{1i}^2 & \sum x_{1i}x_{2i} \\ \sum x_{2i} & \sum x_{1i}x_{2i} & \sum x_{2i}^2 \end{bmatrix} \begin{bmatrix} a_0 \\ a_1 \\ a_2 \end{bmatrix} = \begin{bmatrix} \sum y_i \\ \sum x_{1i}y_i \\ \sum x_{2i}y_i \end{bmatrix}. \quad (\text{B.B0-B.52})$$

Of course the example two-dimensional case can be extended to m dimensions:

$$y = a_0 + a_1x_1 + a_2x_2 + \dots + a_mx_m + e \quad (\text{B.53})$$

where the standard error is formulated as:

$$s_{y/x} = \sqrt{\frac{S_r}{n - (m + 1)}} \quad (\text{B.54})$$

With respect to the experimental data my analysis is a multiple linear regression. The input variable of the various flux models is the net radiation term of the energy balance. I am assuming that the form of the linear equation that fits the data is (the results section, Section 6, will introduce a more complicated version of this equation):

$$Flux = \sum_{i=1}^n a_i (Q^*)^{n_i} + b \quad (\text{B.55})$$

where a_i are the regression coefficients, b is the intercept, Q^* is the net radiation, and n_i are real positive numbers (usually less than 1). Even though there is only one input variable, the analysis is still considered a multiple linear regression because in most cases there are multiple terms with n_i not equal to one. Also, the terms on the right side of Equation B.55 are linearly independent even though they come from the same source.

B.2.4 Non-linear Multiple Regression

In general there are certain cases where the output variable is a function of more than one linearly independent input variable. The setup is similar to that of a linear case but instead of a sum of terms a product is taken as in the following equation.

$$y = a_0 \prod_{i=1}^n x_i + b_0 \quad (\text{B.56})$$

The procedure used to setup the coefficient equations for this case is the same as in previously mentioned cases. The details of this regression method will not be examined here for the same reason. This type of regression is known as non-linear simply for the reason that input variables are multiplied together. Due to the linear independence requirement, there are restrictions on what quantities can be used for this type of analysis. For example, using incoming and outgoing and outgoing short wave radiation will cause a problem since the two quantities are not independent of each other. And, using the same net radiation term but to different powers will also cause problems since the exponents can be combined to form one term.

B.3 Statistica

Using the methods described in the previous section a program named Statistica by Statsoft is used to calculate the regression coefficients. The input for the program is a matrix containing both the independent and dependent variables of the analysis. The multiple regression module of Statistica is capable of implementing simple linear, multiple, forward and backward stepwise, hierarchical, and nonlinear regression models among others. Output of the program is the coefficients of the best fitting terms of a given model and a statistical summary that shows the accuracy of the model. These statistics include standard errors, Beta coefficients, R-squared values, part and partial

correlation matrices, correlations and covariances for regression weights. The following listed statistics are the basis for validating of the models produced by the regression.

B.3.1 Beta weights

Beta is the average amount the dependent variable increases when an independent variable increases one standard deviation and other independent variables are held constant. If an independent variable has a beta weight of 0.5, and when other independents are held constant, the dependent variable will increase by half a standard deviation (0.5). The ratio of the beta weights (with respect to other independent variables) gives the estimated unique predictive importance of the independent variables. Betas will change if variables are added or deleted from the equation since they assess the unique importance of the independent variables relative to the given model. Changes resulting from adding or subtracting variables can be drastic enough to make important independent variables seem unimportant and unnecessary to the analysis. However, reordering the variables without adding or deleting will not affect the beta weights.

B.3.2 t-tests

These tests are used to assess the significance of individual regression coefficients by testing the null hypothesis that the regression coefficient is zero. This test produces a p-value: the probability that the variable is not significant. A common rule of thumb is to eliminate from the equation all variables with a p-value of 0.05 or higher.

B.3.3 R^2

Also called multiple correlation or the coefficient of multiple determination, is the percent of the variance in the dependent explained uniquely by the independents. R-squared can also be interpreted as the proportionate reduction in error in estimating the

dependent when knowing the independents. That is, R^2 reflects the number of errors made when using the regression model to guess the value of the dependent, in ratio to the total errors made when using only the dependent's mean as the basis for estimating all cases. Mathematically,

$$R = \left(1 - \frac{SSE}{SST} \right) \quad (\text{B.57})$$

$$\begin{aligned} SSE &= \sum (y_i - y_{i,est})^2 \\ SST &= \sum (y_i - \bar{y})^2 \end{aligned} \quad (\text{B.58-}$$

B.59)

Thus R^2 is 1 minus regression error as a percent of total error and will be 0 when regression error is as large.

B.3.4 Adjusted R^2

This statistic reflects an adjustment for the fact that with a large number of independents, it is possible that R^2 will become artificially high simply because the variance of some independent variables is a good predictor of small parts of the variance of the dependent variable. The adjustment to the formula arbitrarily lowers R^2 as the number of independents, increases. When used for the case of a few independents, R^2 and adjusted R^2 will be close. When there are a great many independents, adjusted R^2 may be noticeably lower. The greater the number of independents, the more appropriate it is to use the adjusted R^2 . Always use adjusted R^2 when comparing models with different numbers of independents. The adjusted R^2 is calculated by

$$R_{adjusted}^2 = 1 - \left((1 - R^2) \left(\frac{n - 1}{n - k - 1} \right) \right) \quad (B.60)$$

where n is sample size and k is the number of terms in the model.

B.3.5 *F*-test

The purpose of this test is to compare the significance of the difference between two R^2 values. In other words, the F test compares a regression model to the same model with an added independent variable.

$$F = \frac{R_2^2 - R_1^2}{k_2 - k_1} \bigg/ \frac{1 - R_2^2}{n - k_2 - 1} \quad (B.61)$$

where

R_2^2 = R-square for the second model (*e.g.*, one with interactions or with an added independent)

R_1^2 = R-square for the first, restricted model (*e.g.*, without interactions or without an added independent)

n = total sample size

k_2 = number of variables in the second model

k_1 = number of variables in the first, restricted model

F has $(k_2 - k_1)$ and $(n - k_2 - 1)$ degrees of freedom and tests the null hypothesis that the R^2 increment between the two models is not significantly different from zero.

B.3.6 Stepwise Multiple Regression

In addition to the aforementioned statistical analyses, Statistica also has many different types of regression modes. One of the more helpful modes is the stepwise multiple regression. The procedure first selects the most correlated independent, removes

the variance in the dependent variable, then selects the second independent which most correlates with the remaining variance in the dependent, and so on until selection of an additional independent does not increase the R^2 by a significant amount (usually $\text{signif} = .05$). While stepwise regression uses a meaningful criterion for selecting variables, it does not assure that the selected variables will not display high inter-correlation. There are two main options within the stepwise regression. Forward inclusion is the option, usually the default, of entering the best variable first, then the second partially for the first, and so on. Backward elimination is the option of starting with all variables in the equation, and then eliminating independents one at a time until such elimination makes a significant difference in R^2 . Forward inclusion provides a rationale for intelligent but automated ordering of variables but it will miss independents which exhibit suppressor effects -- variables whose significant relationship to the dependent is only apparent when other variables are controlled.

References

- Aubinet, M. *et al.*, 2000: Estimates of the Annual Net Carbon and Water Exchange of Forests. *The EUROFLUX Methodology – Advanced Ecological Research* Vol. 30, pp 113–175.
- Baldocchi, D., 2006: Lecture 2 Micromet Flux Measurements, Eddy Covariance, Part 1, *ESPM 228, Advanced Topics in Biometeorology and Micrometeorology*, Department of Environmental Science, Policy and Management, UC Berkeley
- Beljaars, A. C. M., and A. A. M. Holtslag, 1991: Flux Parameterization Over Land Surfaces for Atmospheric Models. *Journal of Applied Meteorology* Vol 30, 327–341.
- Businger, J. A., Wyngaard, J. C., Izumi, Y., and Bradley, E. F., 1971: Flux Profile Relationships in the Atmospheric Surface Layer. *Journal of Atmospheric Science* Vol 28, pp 181–189.
- Camuffo, D. and Bernardi, A., 1982: An Observational Study of Heat Fluxes and the Relationship with Net Radiation. *Boundary Layer Meteorology* Vol. 23, pp 359–368.
- Clothier, B. E., Clawson, K. L., Pinter, P. J., Jr, Moran, M. S., Reginato, R. J. and Jackson, R. D. 1986: Estimation of Soil Heat Flux from Net Radiation During the Growth of Alfalfa. *Boundary Layer Meteorology* Vol 37, pp 319–329.
- De Bruin, H. A. R. and Holtslag A. A. M., 1982: A Simple Parameterization of the Surface Fluxes of Sensible and Latent Heat During Daytime Compared with the Penman-Monteith Concept. *Journal of Applied Meteorology* Vol. 21, pp 1610 – 1621.
- Dyer, A. J., and Hicks, B. B. 1970: Flux Gradient Relationships in the Constant Flux Layer. *Quarterly Journal of the Royal Meteorological Society* Vol 96, pp 715–721.
- Fritschen, L. J. and Simpson, J. R., 1989: Surface Energy and Radiation Balance Systems: General Description and Improvements. *Journal of Applied Meteorology* Vol. 28, pp 680–689
- Foken, T., Richter, S.H., Muller, H., 1997: The Accuracy of the Bowen Ratio Method. *Weather and Life* Vol. 49, pp 57–77.
- Gorsevski, V., Taha, H, and Quattrochi, D., 1998: Air Pollution Prevention Through Urban Heat Island Mitigation: Ann Update on the Urban Heat Island Pilot Project.

- Grimmond, C. S., Cleugh, H. A., and Oke, T. R., 1991: An Objective Urban Heat Storage Model and its Comparison with other Schemes, *Atmospheric Environment*, Vol. 25B, NO. 3., pp 311-326
- Hicks, B. B., 1976: Wind Profile Relationships from the 'Wangara' Experiments. *Quarterly Journal of the Royal Meteorological Society* Vol 102, pp 535-551.
- Holtzlag, A. A. M., and DeBruin, H. A. R., 1988: Applied Modeling of the Nighttime Surface Energy Balance Over Land. *Journal of Applied Meteorology* Vol 27, pp 689-704.
- Holtzlag, A.A.M. and Van Ulden, A.P., 1983: A Simple Scheme for Daytime Estimates of the Surface Fluxes from Routine Weather Data, *Journal of Climate and Applied Meteorology*, Vol. 22, NO.4, April, pp 517-529
- Horace, R., 1959: General Meteorology, 3rd Edition, McGraw-Hill Book Company Inc.
- Liu, H. and Foken, T., 2000: A Modified Bowen Ratio Method to Determine Sensible and Latent Heat Fluxes, *Meteorologische Zeitschrift*, Vol. 10, NO. 1, pp 71-80
- Oke, T. R., Kalanda, B. D. and Steyn, D. G. 1981: Parameterization of Heat Storage in Urban Areas, *Urban Ecology* , Vol. 5, pp 45-54
- Oke, T. R. and Cleugh, H. A., 1987: Urban Heat Storage Derived as Energy Budget Residuals. *Boundary Layer Meteorology* Vol. 39, pp 223-245
- Panofsky, H. A. and Dutton, J. A. 1984: *Atmospheric Turbulence, Models and Methods for Engineering Applications*, John Wiley & Sons, New York.
- Paulson, C. A., 1970: The Mathematical Representation of Wind Speed and Temperature Profiles in the Unstable Atmospheric Surface Layer. *Journal of Atmospheric Science* Vol 9, pp 856-861.
- Smith, F.B., and Blackall, R. M., 1979: The Application of Field Experimental Data to the Parameterization of the Dispersion of Plumes from Ground Level and Elevated Sources. *Mathematical Modeling of Turbulent Diffusion in the Environment*, J. Harris Ed., Academic Press, p 500.
- Stewart, J.B. and Thom, A.S., 1973: Energy Budgets in Pine Forest. *Quarterly Journal of the Royal Meteorological Society* Vol 99, pp. 154-170.
- Wieringa, J. 1976: An Objective Exposure Correction Method for Average Wind Speeds Measured at a Sheltered Location. *Royal Meteorological Society Quarterly Journal* Vol 102, pp 241-253

- Xu, Q., and Qiu, C. 1997: A Variational Method for Computing Surface Heat Fluxes from ARM Surface Energy and Radiation Balance Systems. *Journal of Applied Meteorology* Vol 36, pp 3–11.
- Zhang, S., Qiu, C., and Zhang, W., 2004: Estimating Heat Fluxes by Merging Profile Formulae and the Energy Budget with a Variational Technique, *Advances in Atmospheric Sciences*, Vol 21, NO. 4, pp. 627-636
- Campbell Scientific, Inc: CR 5000 Measurement and Control System Overview, Copyright 2001
- Campbell Scientific, Inc: CNR1 Net Radiometer Instruction Manual, Copyright, 2004
- Campbell Scientific, Inc: CSAT3 Three Dimensional Sonic Anemometer Instruction Manual, Copyright 1998
- Campbell Scientific, Inc: CS616 Water Content Reflectometer Instruction Manual, Copyright 2004
- Campbell Scientific, Inc: Eddy Covariance System CA27 and KH20 Instruction Manual, Copyright 1998
- Campbell Scientific, Inc: Model HFP01SC Self-Calibrating Soil Heat Flux Plate, Copyright 2005
- Campbell Scientific, Inc: Model HMP45C Temperature and Relative Humidity Probe Instruction Manual, Copyright 2002
- Campbell Scientific, Inc: IRTS-P Precision Infrared Temperature Sensor, Copyright 2005